

TECHNICAL UNIVERSITY OF CRETE  
ELECTRICAL AND COMPUTER ENGINEERING DEPARTMENT  
TELECOMMUNICATIONS DIVISION



# Low-Cost Software-Defined Radios (SDR) & Techniques for Robotic RFID Systems

by

Konstantinos Skyvalakis

A THESIS SUBMITTED IN PARTIAL FULFILLMENT OF  
THE REQUIREMENTS FOR THE MASTER OF  
ELECTRICAL AND COMPUTER ENGINEERING

July 2021

THESIS COMMITTEE

Professor Aggelos Bletsas, *Thesis Supervisor*

Professor George N. Karystinos

Professor Michael Paterakis

*In loving memory of my beloved grandmother, Maria.*

# Abstract

The continuously increasing deployment of RFID tags has sparked strong academic and industrial interest on improved RFID tag throughput and localization. This work proposes a collision resolution method to boost the inventorying capacity of RFID readers, as well as a novel phase-based method for multistatic 2D/3D localization. The first part of this thesis proposes a Viterbi joint sequence detector that can resolve a collision between two tags in the physical layer. In sharp contrast to prior art, the proposed closed-form signal model takes into account the asynchrony level between the two collided tag responses, which is not uncommon with commercial, ultra-low-cost RFID tags that follow industry's Gen2 protocol. Asynchrony is considered as the time offset  $\tau$  between the beginnings of the two tags' responses and is modeled through a derived shaping matrix that depends on the delayed tag information. Performance evaluation of the proposed detectors with simulated data under Ricean fading, as well as experimental data with software-defined radio (SDR), reveals improved performance compared to prior art, under various operating regimes. It is also shown that for different values of the parameter  $\tau$ , BER does not present a monotonic behavior. As a collateral dividend, it is found that clustering techniques on the filtered received signal should explicitly take into account the time offset  $\tau$ , since the latter modifies the number of observed clusters. The second part of this thesis offers elliptical direction-of-arrival (DoA) estimation and 2D/3D localization techniques, using phase-based, narrowband measurements. The method exploits a multistatic architecture, where illuminating and receiving antennas are placed in the same line. Ambiguities inherent in phase measurements are analytically addressed. Experimental results with Gen2 UHF RFID tags show similar performance in terms of DoA estimation compared to the MUSIC algorithm. In terms of 2D localization accuracy, the proposed method outperformed state-of-the-art algorithms in all experimental cases at the lab, offering mean absolute localization error as small as 9 cm, at the expense of additional effort for calibration. As a collateral dividend, proof-of-concept is offered via simulation that the multistatic 2D localization method, could

---

possibly be applied in real-time motion tracking of a mobile robotic platform equipped with a Gen2 UHF RFID tag. Extension of the localization method for the 3D case is also offered, with promising simulation results.

# Acknowledgements

First and foremost, I am extremely grateful to my supervisor, Prof. Aggelos Bletsas, for offering me his invaluable advice, continuous support, and patience during my MSc studies. My gratitude and appreciation extends to my family as well, for their constant and unconditional love and support and of course, my partner Evgenia; she has been by my side for many years now, supportive and encouraging through good and bad times. I would also like to thank my friends and colleagues at the lab, Giorgos, Vaggelis, Manos, Iosif and Spyros for the fun times we had together and their invaluable help throughout this thesis work.



This research has been cofinanced by the European Union and Greek national funds through the Operational Program Competitiveness, Entrepreneurship and Innovation, under the call RESEARCH - CREATE - INNOVATE (project code: T1EDK-03032).

# Contents

<b>Abstract</b> . . . . .	3
<b>Acknowledgements</b> . . . . .	5
<b>1 Introduction</b> . . . . .	9
1.1 RFID Technology . . . . .	9
1.2 RFID Applications in Robotic Systems . . . . .	14
1.3 Thesis Organization & Contributions . . . . .	17
1.4 Notation . . . . .	18
<b>2 Asynchronous Reception of 2 Gen2 RFID Tags</b> . . . . .	19
2.1 System Model . . . . .	20
2.1.1 Channel Model . . . . .	20
2.1.2 Signal Model . . . . .	21
2.1.3 FM0 Line Coding . . . . .	22
2.2 Problem Transformation . . . . .	24
2.2.1 Number of Clusters . . . . .	25
2.2.2 SNR Calculation . . . . .	26
2.3 Detection Techniques . . . . .	27
2.3.1 $T$ Detection for Tag $b$ . . . . .	28
2.3.2 $2T$ Detection for Tag $a$ . . . . .	28
2.3.3 $2T$ Detection for Tag $a$ and Tag $b$ . . . . .	29
2.3.4 Viterbi . . . . .	29
2.3.5 Zero-Forcing . . . . .	31
2.4 Digital Link Housekeeping . . . . .	32
2.4.1 DC Estimation . . . . .	32
2.4.2 Channel Estimation . . . . .	32
2.4.3 Time Offset Estimation . . . . .	33

---

<b>3</b>	<b>Simulation &amp; Experimental Evaluation of Asynchronous Reception</b>	35
3.1	Simulation Results . . . . .	35
3.2	Experimental Evaluation using Software-Defined Radio (SDR) . . . . .	39
3.3	Discussion . . . . .	41
<b>4</b>	<b>Multistatic Localization of Gen2 RFID Tags</b> . . . . .	42
4.1	System Model . . . . .	43
4.1.1	Phase-Based Preliminaries . . . . .	44
4.2	Direction-of-arrival Techniques for RFID Tag Signals . . . . .	45
4.2.1	MULTiple SIGNAL Classification (MUSIC) . . . . .	45
4.2.2	Multistatic Direction-of-Arrival (ElIDoA) . . . . .	47
4.3	Multistatic 2D Localization . . . . .	51
4.4	Multistatic 3D Localization . . . . .	52
<b>5</b>	<b>Simulation &amp; Experimental Evaluation of Multistatic Localization</b>	55
5.1	Experimental Evaluation of MUSIC and ElIDoA . . . . .	55
5.2	Simulation Results of 2D Localization . . . . .	57
5.3	Experimental Evaluation of 2D Localization Algorithm for RFID Tags	60
5.4	Simulation Results of 3D Localization . . . . .	62
5.5	Discussion . . . . .	63
<b>6</b>	<b>Conclusion</b> . . . . .	64
6.1	Summary of Thesis Contributions . . . . .	64
6.2	Direction for Future Work . . . . .	65
<b>7</b>	<b>Appendix</b> . . . . .	66
7.1	Appendix of Chapter 2 . . . . .	66
7.1.1	Proof of Theorem 1 . . . . .	66
7.1.2	Proof of Eq. (2.18) . . . . .	68
7.1.3	Proof of Eq. (2.20) . . . . .	69
7.2	Appendix of Chapter 4 . . . . .	70
7.2.1	Intersection of 2 Conic Sections . . . . .	70
7.2.2	Proof of ElIDoA . . . . .	74
7.3	Appendix of Chapter 5 . . . . .	75
7.3.1	Synchronization of 2 USRP N200 SDRs using UHD Timed Commands . . . . .	75

---

**References** ..... 78

# Chapter 1

## Introduction

### 1.1 RFID Technology

A lot of positive attention has recently been paid to Radio Frequency Identification (RFID) tags and Internet-of-Things(IoT), which keep on having a huge impact in our daily lives. Their ultra-low-cost of production and efficient way of operation without utilizing a battery as energy source, has made them a cheap and trustworthy solution for numerous applications. Such applications range from inventory control in a warehouse and public transportation tickets to animal tracking and robotic systems.

In order to interrogate an RFID tag and obtain its unique identification number (EPC), an RFID reader is required. RFID readers themselves are separated into two major categories, monostatic and multistatic. In monostatic RFID readers, a single device performs both transmission and reception tasks, while in multistatic RFID readers, multiple devices are utilized, some for transmission and some others for reception. Multistatic RFID readers though suffer from carrier frequency offset (CFO) that monostatic readers do not; however, coverage range is widely increased when multistatic architecture is utilized.

An RFID reader operates according to the policies dictated by the Gen2 protocol, [1]. The principle of operation of RFID tags is quite simple and is based on backscatter communication. An RFID tag, when illuminated (energized) by an RF source, acts like the example of the mirror and the flashlight, where by tilting the mirror, the incident light gets reflected back or not. More specifically, each RFID tag terminates its antenna between two loads; load  $Z_0$  open-circuits the tag antenna, thus, the tag absorbs no energy and maximizes its reflection coefficient, while in state  $Z_1$  "perfect" matching occurs, resulting in maximum power transfer for RF energy harvesting, reducing the reflection coefficient to zero.

Gen2 RFID tags can be either active, semi-passive (battery-assisted) or passive (i.e., not equipped with a battery). Such passive RFID tags solely rely on harvesting energy from the incident RF wave, as already mentioned above. Thus, to ensure the

tag will always power up and transmit its EPC ID, regardless of the backscattered bit sequence, line codes are utilized. Such line codes used in Gen2 tags are FM0 and Miller 2/4/8, which force the tags to switch between the two loads on a 50% duty cycle, ensuring energy harvesting for every possible backscattered sequence.

With the constantly increasing number of deployed batteryless radio frequency identification (RFID) / internet-of-things (IoT) tags, academic and industrial research interest has lately been focused on ways to accelerate the inventorying process and improve efficiency and throughput.

The commercial Gen2 standard [1], utilizes the framed slotted Aloha (FSA) algorithm to facilitate *tag singulation*. RFID tags *compete* by transmitting a pseudo-random 16-bit sequence each (plus common 6 preamble bits), named as RN16; the tag that *wins* the slot, transmits its ID information (EPC) in a subsequent time step, while the rest of the competing tags are waiting for their turn in a next slot. When two or more tags respond simultaneously inside the same slot, the tags' RN16 packets collide mid-air, which typically results to incorrect detection, since the reader cannot detect a single correct RN16 sequence to acknowledge; in that case, no tag transmits its EPC and a whole frame is wasted, resulting to inventorying rate drop. Thus, collision among two or more tags can only occur during the RN16 transmission stage and it only makes sense that anti-collision techniques should focus directly on the physical layer of communication. Fig. 1.1-left depicts such collision case, with inphase (I) and quadrature (Q) signals collected experimentally; the reader transmits a query, 2 tags respond at the same slot, the RN16 is not decoded properly at the reader and no tag receives a valid acknowledgement with its transmitted RN16 information; thus, no tag transmits its ID information (EPC) subsequently.

Assuming FSA with  $N$  tags competing for  $L$  slots, the probability of exactly  $q$  tags (out of  $N$ ) choosing the same slot is simply given through the binomial:  $\Pr(q) = \binom{N}{q}(1/L)^q(1-1/L)^{N-q}$ . Therefore, the probability of collision is given by  $\Pr(q=2) + \Pr(q=3) + \dots = \sum_{q=2}^{\infty} \Pr(q)$ . In a practical scenario, where the reader selects a relatively large number of slots, the collision probability is dominated by  $\Pr(q=2)$ , i.e., the probability that exactly two tags' RN16 information is transmitted at the same slot. Specifically, probability of more than two tags (i.e., *at least* three tags) collide at the same slot  $\sum_{q=3}^{\infty} \Pr(q) = 1 - \Pr(q=0) - \Pr(q=1) - \Pr(q=2)$  is given at Fig. 1.2, for various number of tags  $N$  and slots  $L$ ; it can be safely said that collision probability of more than 2 tags drops below 1% for reasonable numbers of  $N, L$ . What is more, according to the Gen2 protocol, even if the reader could

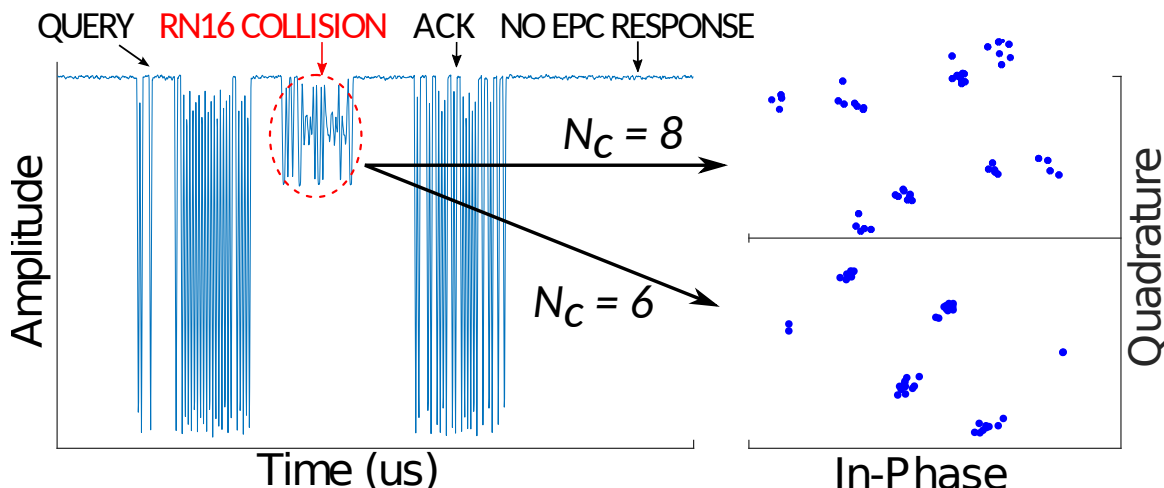


Figure 1.1: RN16 collision of 2 tags resulting in 6 or 8 clusters. Plot was offered after experimentation with 2 commercial tags and the software stack from work in [2].

correctly detect all tags' RN16 information, it would acknowledge only one of them; thus, better joint detection of all collided tags would not necessarily offer increased throughput. Therefore, the case of 2 tag's collision in Gen2 is important, *both* from a theoretical *and* practical standpoint.

This work, investigates the 2 RFID tags collision resolution problem in the context of increasing the throughput of the reader attached on our laboratory's robotic platform. The mobile robotic platform of our laboratory is, besides others, equipped with a USRP N200 SDR device implementing an RFID reader, [2], to interrogate Gen2 RFID tags. The task of the mobile robotic platform is to roam around inside a warehouse building or a library and interrogate RFID tags, with the ultimate purpose of localizing them. However, in such tag-crowded environments collisions are a very often occurrence; thus, the collision resolution problem is studied in an effort to increase the efficiency and throughput of the RFID reader equipped on the robot. As a collateral dividend, the rate at which tags are interrogated would increase and more measurements would be available in a shorter time period for the localization algorithms.

Following the high demand for successful inventorying of backscatter-based tags and sensors, as quickly and efficiently as possible, prior art [3] has analyzed the I/Q constellation of tag signals colliding in a single slot, leveraging clustering techniques for up to four colliding tag signals. However, this work was initially developed for low frequency (LF) tags and could perhaps be extended to Gen2 RFID tags. The authors in [4], [5] proposed a zero-forcing (ZF) receiver that treats one of the two tag's

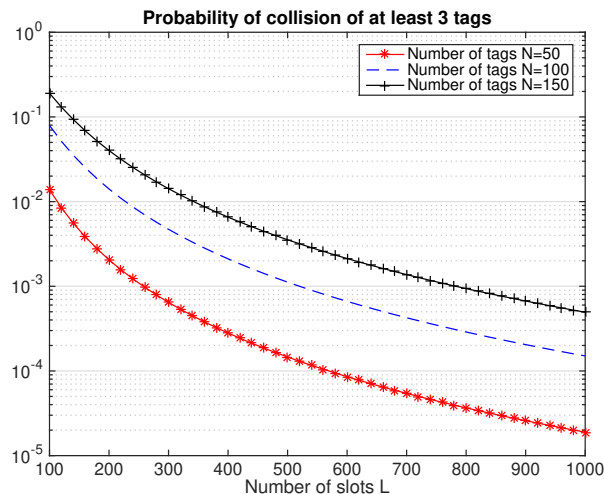


Figure 1.2: Probability of collision of more than 2 tags (i.e., 3 or more) in slotted Aloha of  $L$  slots, among  $N$  tags. Notice that such probability can drop below 1% for reasonable numbers of  $N$  and  $L$ .

RN16 responses as interference, and projects the signal constellation into the subspace that completely cancels that interference. Work in [6, 7] proposed ZF and minimum mean squared error (MMSE) receivers, exploiting multiple receiving antennas and additional reference bits, not currently present in Gen2, that could assist channel estimation.

Work in [8] proposed a detection technique for collision of multiple FM0 or Miller RFID line-encoded signals, based on *single-tag* Viterbi detector and successive interference cancellation (SIC). Initially, a single tag reply is assumed and an estimate of the symbol period and the delay offset is obtained by employing a correlation-based method. Then, *single-tag* maximum likelihood sequence detector (i.e., Viterbi) is applied to decode the single tag's information, in sharp contrast to this work, which designs a *joint* Viterbi detector for *both* tags. Finally, an estimate of the tag's contribution is generated and subtracted from the residual and the same process is repeated until termination. As in every SIC-based technique, the above method is sensitive to the power ratio among the tags. Work in [9] proposed multiple access based on rateless codes, which is closer to code division multiple access (CDMA). Frequency domain multiple access (FDMA), based on different subcarrier per tag, i.e., different switching rate of each tag among two termination loads, has been proposed and experimentally demonstrated in [10] using minimum shift keying (MSK), also showcasing that efficient spectrum shaping can be achieved with only two loads per tag and a

common carrier frequency at the reader. Both aforementioned techniques depart from the time division multiple access (TDMA) concept of FSA in Gen2.

Work in [11, 12] proposed a new protocol (different than Gen2), resolving tag collisions by separating the signals' edges in the time domain, while also leveraging the I/Q samples to further clarify any ambiguities that might occur due to the asynchronous character of the system. Work in [13] follows a similar approach to [12] but focuses on Gen2. In [14], the authors claim that the signals' combined states follow highly stable probabilities; transitions between the clusters in the I/Q plane are tracked, decoding the individual packets involved in the collision, without the need to track signals' edges in the time-domain. Work in [14] is extended in [15], which proposes exploitation of the spatiotemporal distribution of the collided signals. Finally, work in [16] proposes a multi-antenna blind beamforming technique, which however does not take into account the impact of asynchrony on the number of observed I/Q clusters.

In sharp contrast to prior art, this work offers a closed-form system model, which explicitly takes the time offset between the responses of the two tags into consideration, rather than neglecting it. Even though the tags always respond to the reader commands, it has been experimentally most likely due to their ultra-low cost hardware. The offered detectors are built upon the proposed closed-form signal model and take into account the time offset between the two tags, modelled through the use of a shaping matrix. Given that all reception techniques involve some type of filtering to improve signal-to-noise (SNR) ratio (e.g., matched filtering), plotting the filtered samples of the received signal offers information about the existence of such asynchrony.

More specifically, a collision in the physical layer between two Gen2 RFID tag RN16 responses, can either result in 4, 6 or 8 clusters in the I/Q plane, *after* matched filtering of the received signal and then, plotting the real and imaginary part, experimentally shown in Fig. 1.1-right and explained through formal proofs in this work. Fig. 1.1 was offered after experimentation with commodity software-defined radio (SDR) and Gen2 RFID tags. After matched filtering, 4 clusters can be observed when the 2 tags appear to be perfectly time-synchronized (i.e., time offset is zero or  $T/2$ ), while the 6 and 8 clusters cases, also shown in Fig. 1.1, occur for the remaining time offset values between 0 and  $T$ . Thus, collision resolution based on clustering methods should take into account such reality. Extensive experimental tests at the lab, interrogating 10000 times 2 commercial Gen2 RFID tags corroborated the

above: 57% of the time the 2 tags were out of sync, while 98% of those asynchronous collisions generated more than 4 clusters on the I/Q plane, after matched filtering.

## 1.2 RFID Applications in Robotic Systems

Localization of wirelessly powered devices such as RFID tags is essential for many applications related to the Internet of Things and Ubiquitous Computing. Utilization of mobile robotic platforms to perform such a task seems to be inevitable. A use case of RFID in robotics could be for example in a industrial warehouse. Assume a big industrial warehouse building, where packages are stacked on top of each other on shelves spanning the whole length of the warehouse. Assigning the inventorying task to some workers is going to be a painstakingly slow process and will definitely last way longer than if just some sort of mobile robotic platform was used. Thus, while the robot is performing the inventorying process, the workers' skills could be better utilized in some other more meaningful task.

The robotic platform of our laboratory, Fig. 1.3, is equipped with an on-board computer, a monostatic RFID reader, antennas and a LiDAR to localize itself according to the surrounding environment data. The task of such a mobile robotic platform would be to move between the shelves (e.g., in a warehouse, a library or a supermarket) and interrogate the RFID tags attached on the items (e.g., packets, books). Backscattered signal phase measurements obtained from the transaction with the RFID tags, would then be processed on the robot's on-board Intel NUC computer to extract each interrogated tag's 2D/3D location inside the area of operation, [17].

For years now, the Global Positioning System (GPS) has demonstrated extraordinary performance in localizing targets all over the earth. However, the trade-off of GPS is, that when the target moves inside a building or underground, the localization accuracy is obviously poorer; in some cases localization is not even possible. When the error is large, the whole localization system loses its practical significance and thus, the need for indoors localization has been revisited the last few years, especially now with all the robotic platforms and drones deployed in numerous indoors applications. One cheap and efficient way to localize known targets indoors, would be by attaching an RFID tag onto them and exploiting various 2D/3D localization techniques, such as the ones offered in this work, to track their location at all times.

Apart from tracking mobile or static targets indoors, the usage of RFID tags, in the context of IoT development throughout these last years, could be hugely optimized



Figure 1.3: Kobuki TurtleBot 2 mobile robotic platform, equipped with a monostatic RFID reader.

if identification information was linked to location data. Now, more than ever, with the rise of 5G and all the promising IoT applications, such as smart cars, smart homes etc., localization of RFID tags is regarded as a key enabler for this technology.

In order to interrogate an RFID tag and later run a localization algorithm based on the received signal, the tag needs to be situated in the coverage field of a monostatic RFID reader (i.e., an RFID reader that utilizes a single device for reception/transmission). However, a more efficient and robust method to extend the operational range of Gen2 RFID tags is via multistatic radio, as opposed to just increasing the transmission power of the monostatic reader. Prior findings on bistatic [18], [19–23] or multistatic [24] backscatter radio have shown how such architectures can effectively boost the range of telecommunications. By exploiting the dyadic [25], non-linear nature of wireless propagation, link budget and diversity gain can be achieved [24]. Thus, a multistatic setup has tremendous advantages over its monostatic counterpart, albeit with increased installation cost.

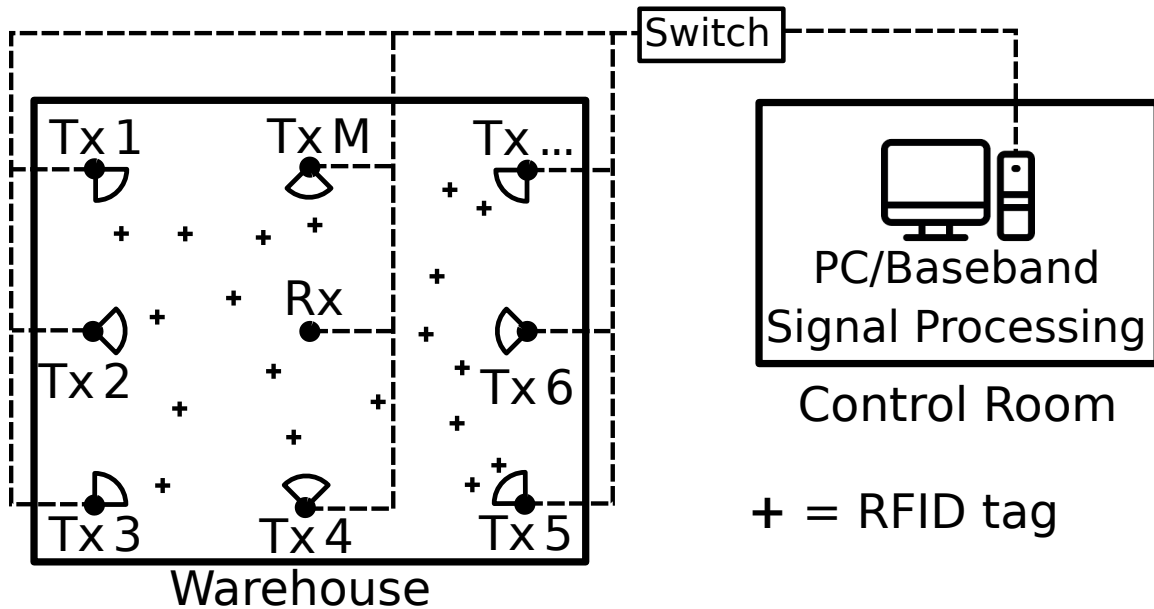


Figure 1.4: Deployment of multiple SDR transmitters/illuminators along with a single receiving SDR in a warehouse, [26], implementing a multistatic RFID reader.

It should be noted, that the proposed multistatic architecture is impacted from the timing constraints of the Gen2 protocol more severely than its monostatic counterpart. This is because baseband packet communication is performed through an Ethernet layer, as well as the fact that the signal processing and control logic is running on software (instead of hardware). As a result, all signal processing algorithms need to be fast and robust in order to reliably interrogate passive Gen2 RFID tags.

One of the numerous applications of multistatic scatter radio is in the localization of a mobile robotic platform. In that case, the robot would be equipped with a Gen2 RFID tag; a multistatic RFID reader such as the one portrayed in Fig. 1.4, would be utilized to measure the phase of the signal backscattered from the tag. As it will be shown in depth later on in this chapter, phase measurements obtained from a multistatic RFID reader, can facilitate 2D localization of RFID tags. Typically, multistatic architecture utilizes multiple transmitting SDRs and a single receiving SDR. The transmitting SDRs take turns, according to some scheduling algorithm (e.g., Round Robin), illuminating the tags in their vicinity. Hence, most if not all of the RFID tags inside the warehouse would eventually be inventoried, as opposed to a typical monostatic RFID reader that would only cover a fraction of the area. Being able to cover larger spaces with such multistatic setups, could potentially facilitate the localization of mobile robotic platforms through multiple rooms and/or levels

inside the operating environment.

Since RFID localization has been attracting considerable excitement within the relative research communities, phase-based techniques have recently appeared in the RFID localization literature [27–34].

Phase measurements introduce by definition an ambiguity in distance, measured in wavelength multiples (for one-way wireless communication) or half-wavelength multiples (for round-trip backscatter communication). The latter can be mitigated by exploiting various wavelengths and increased bandwidth [35] or mobility, i.e., taking measurements at multiple positions, with either the tags or the reader in motion [28], [31–34]. RFID reader mobility imposes additional adversities, such as estimating or knowing a-priori the location of the reader [33]. Work in [36] includes direction-of-arrival (DoA) estimation through mobility of the reader or reference tags at known locations (e.g. [32], [36]), to estimate the location of a tag. Furthermore, RFID tag localization based on excessive bandwidth has been also proposed by the authors in [37]. Super-resolution techniques based on tens of megahertz bandwidth and multi-antenna terminals have been also studied in the context of wireless CSI-based WiFi localization [38]. Even though excessive bandwidth can offer impressive localization results, Gen2 RFID operation (e.g., in European UHF ISM bands) is not compatible with such excessive bandwidth requirements. Finally, our group’s work in [17], utilizes a particle filtering method to facilitate 2D/3D tag localization. The latter introduces a different distance metric of each particle-measurement phase pair, based on geometry arguments, which is more robust to phase measurement noise (e.g., due to multipath) compared to other phase-based localization methods.

## 1.3 Thesis Organization & Contributions

In this section we jointly outline the organization of this thesis and its key contributions.

In **Chapter 2**, a novel system model for the simultaneous asynchronous reception of 2 RFID tags, is provided. Furthermore, DC, channel and delay offset estimation techniques are offered along with various joint and single tag detection schemes.

In **Chapter 3**, the simulation and experimental evaluation of the collision resolution algorithms offered in **Chapter 2** takes place, utilizing a USRP N200 SDR device.

In **Chapter 4**, a DoA estimation technique and a multistatic 2D/3D localization algorithm for RFID tags is offered, utilizing phase measurements from a multistatic RFID reader.

In **Chapter 5**, the simulation and experimental evaluation of the DoA and the multistatic 2D/3D localization algorithms offered in **Chapter 4** is conducted, this time utilizing two USRP N200 SDR devices.

In **Chapter 6**, we conclude this thesis, and provide directions for future work and possible extensions to our solutions.

## 1.4 Notation

Symbols  $\mathbb{N}$ ,  $\mathbb{R}$ , and  $\mathbb{C}$  denote the set of natural, real, and complex numbers, respectively.  $\mathbf{0}_N$  and  $\mathbf{I}_N$ , denote the all-zeros vector and identity matrix of size  $N$ , respectively. The phase of complex number  $z$  is denoted as  $\angle z$ , while  $\Re\{z\}$  and  $\Im\{z\}$  denote the real and imaginary part of  $z$ , respectively.  $\mathbf{x}^H$  denotes the conjugate transpose (Hermitian) of complex vector  $\mathbf{x}$ . The distribution of a proper complex Gaussian  $N \times 1$  vector  $\mathbf{x}$  with mean  $\boldsymbol{\mu}$  and covariance matrix  $\boldsymbol{\Sigma}$  is denoted by  $\mathcal{CN}(\boldsymbol{\mu}, \boldsymbol{\Sigma}) \triangleq \frac{1}{\pi^N \det(\boldsymbol{\Sigma})} e^{-(\mathbf{x}-\boldsymbol{\mu})^H \boldsymbol{\Sigma}^{-1} (\mathbf{x}-\boldsymbol{\mu})}$ ; the special case of a circularly symmetric complex Gaussian  $N \times 1$  vector corresponds by definition to  $\mathcal{CN}(\mathbf{0}_N, \boldsymbol{\Sigma})$ ;  $\mathcal{U}[a, b)$  denotes the uniform distribution in  $[a, b)$ . The Euclidean norm of complex vector  $\mathbf{x}$  is denoted as  $\|\mathbf{x}\|_2 = \sqrt{\mathbf{x}^H \mathbf{x}}$ . Expectation of function  $g(\cdot)$  of continuous random variable  $x$  with probability density function (PDF)  $f_x(\cdot)$  is denoted as  $\mathbb{E}[g(x)] \triangleq \int_x g(x) f_x(x) dx$ . The probability of event  $\mathcal{A}$  is denoted as  $\mathbb{P}(\mathcal{A})$ ;  $\mathbf{1}(\mathcal{C})$  denotes the indicator function, which equals 1 when condition  $\mathcal{C}$  is true and 0 otherwise.

# Chapter 2

## Asynchronous Reception of 2 Gen2 RFID Tags

This chapter contributes to 2 tags asynchronous simultaneous reception in the following aspects:

- Detection techniques are offered that explicitly take into account the time offset  $\tau$  (asynchrony) between two tags;
- It is shown that the proposed asynchronous detection techniques with estimated CSI and  $\tau$  can offer BER in certain regimes that renders the detection of the 16 bits from one of the two tags RN16 message, error free. Moreover, the value of  $\tau$  in the detectors' performance is important and presents an oscillating behaviour;
- It is shown that there exists a small performance gap of the proposed detectors that utilize signal duration of 2 symbols, compared to Viterbi for joint tag detection in the asynchronous case; such performance gap is relatively small and due to the extra induced memory from the delayed second tag; it was also found that the proposed  $2T$  detectors performed as well as Viterbi in the synchronous case;
- Practical algorithm for time offset estimation is offered. It is shown that symbol detection, packet synchronization and channel estimation must be revisited in asynchronous multiple access systems, as in this work;
- As a collateral dividend, it is shown that clustering techniques on the *filtered* received signal should explicitly take into account the time offset  $\tau$ , that modifies the number of observed clusters;

### Chapter Organization

The rest of this chapter is organized as follows. Section 2.1 offers the system model; Section 2.2 presents transformation of the problem; Section 2.3 offers the detection

techniques; finally, Section 2.4 offers necessary housekeeping, i.e., DC, channel and delay estimation techniques utilized in this work.

## 2.1 System Model

### 2.1.1 Channel Model

The following *large-scale* channel path-loss model is adopted [39]:

$$L_k = \left( \frac{\lambda}{4\pi d_0} \right)^2 \left( \frac{d_0}{d_k} \right)^{v_k}, \quad (2.1)$$

where  $k \in \{\text{CR}, \text{CT}_m, \text{T}_m\text{R}\}$  denotes the carrier emitter-to-reader, carrier emitter-to-tag and tag-to-reader link, respectively,  $\lambda$  is the carrier wavelength,  $d_0$  is a reference distance and  $v_k$  is the path-loss exponent for link  $k$ . Moreover, a monostatic setup is assumed, corresponding to  $L_{\text{CT}_m} = L_{\text{T}_m\text{R}}$ .

Due to strong line-of-sight (LoS) signals present in this problem, *small-scale* Rice flat fading channel model [39] is adopted; end-2-end complex channel gain for tag  $m \in \{a, b\}$  is denoted as follows:

$$h_m = h_{\text{CT}_m} h_{\text{T}_m\text{R}} = |h_{\text{CT}_m} h_{\text{T}_m\text{R}}| e^{-j\phi_m} \in \mathbb{C}, \quad (2.2)$$

where  $h_{\text{CT}_m}$  and  $h_{\text{T}_m\text{R}}$  denotes the baseband complex channel coefficients for the carrier emitter-tag and tag-reader link, respectively; furthermore,  $h_m \in \mathbb{C}$ ,  $|h_{\text{CT}_m} h_{\text{T}_m\text{R}}| \in \mathbb{R}_+$  and  $\phi_m \in [0, 2\pi)$ . Due to the assumed monostatic architecture, reciprocity implies  $h_{\text{T}_m\text{R}} = h_{\text{CT}_m}$  and due to the Rice channel fading assumption,

$$h_{\text{T}_m\text{R}} \sim \mathcal{CN} \left( \sqrt{\frac{\kappa_m}{\kappa_m + 1}} \sigma_{h_{\text{T}_m\text{R}}}, \frac{\sigma_{h_{\text{T}_m\text{R}}}^2}{\kappa_m + 1} \right), \quad (2.3)$$

where  $\mathbb{E}[|h_{\text{T}_m\text{R}}|^2] = \sigma_{h_{\text{T}_m\text{R}}}^2$  is the average power of the scattering components and  $\kappa_m = k_{\text{T}_m\text{R}} = k_{\text{CT}_m}$  is the power ratio between the deterministic LoS component and the scattering components. For link budget normalization purposes,  $\mathbb{E}[|h_m|^2] = \mathbb{E}[|h_{\text{T}_m\text{R}}|^4] = 1$  will be also assumed.

### 2.1.2 Signal Model

The reader transmits a sinusoidal carrier wave (CW), whose complex baseband equivalent representation is given by:

$$c(t) = \sqrt{2P_c} e^{-j(2\pi\Delta F t + \Delta\phi)}, \quad \Delta\phi \sim \mathcal{U}[0, 2\pi), \quad (2.4)$$

where  $\Delta F$ ,  $\Delta\phi$  denotes the carrier frequency offset (CFO) and the phase offset, respectively, compared to the receiver and  $P_c$  the power of the carrier wave. Two tags will be assumed: tag  $a$  and tag  $b$ . The baseband complex equivalent of the scattered waveform from tag  $m \in \{a, b\}$  is given by, [19]:

$$u_m(t) = \sqrt{\eta \mathcal{L}_{CT_m}} [(A_s - \Gamma_0) + (\Gamma_0 - \Gamma_1)x_m(t)] h_{CT_m} c(t), \quad (2.5)$$

$$h_{CT_m} = |h_{CT_m}| e^{-j\phi_{CT_m}}, \quad \phi_{CT_m} \in [0, 2\pi), \quad (2.6)$$

where  $x_m(t) \in \{0, 1\}$ ,  $\eta$  models tag power scattering efficiency and  $\Gamma_0, \Gamma_1$  stands for the reflection coefficients for bit "0" and bit "1", respectively; parameter  $A_s$  stands for the load-independent *structural mode* that solely depends on tag's antenna [40].

For the duration  $T$  of a single bit, the received demodulated complex baseband signal at the SDR reader is given by the superposition of the carrier emitter (CE) sinusoid and the tags' backscattered signals propagated through wireless channels  $h_{CR}$  and  $h_{T_mR}$ , respectively:

$$\begin{aligned} y(t) &= \sqrt{\mathcal{L}_{CR}} |h_{CR}| e^{-j\phi_{CR}} c(t) + \sqrt{\mathcal{L}_{T_aR}} |h_{T_aR}| e^{-j\phi_{T_aR}} u_a(t) \\ &+ \sqrt{\mathcal{L}_{T_bR}} |h_{T_bR}| e^{-j\phi_{T_bR}} u_b(t) + n(t) \\ &= \left[ \sqrt{2P_c} e^{-j\Delta\phi} \left( \sqrt{\mathcal{L}_{CR}} |h_{CR}| e^{-j\phi_{CR}} \right. \right. \\ &+ \sqrt{\eta \mathcal{L}_{CT_a} \mathcal{L}_{T_aR}} (A_s - \Gamma_0) |h_{CT_a} h_{T_aR}| e^{-j(\phi_{CT_a} + \phi_{T_aR})} \\ &+ \left. \left. \sqrt{\eta \mathcal{L}_{CT_b} \mathcal{L}_{T_bR}} (A_s - \Gamma_0) |h_{CT_b} h_{T_bR}| e^{-j(\phi_{CT_b} + \phi_{T_bR})} \right) \right. \\ &+ \sqrt{2\eta P_c} (\Gamma_0 - \Gamma_1) \left( \sqrt{\mathcal{L}_{CT_a} \mathcal{L}_{T_aR}} |h_{CT_a} h_{T_aR}| e^{-j\phi_a} x_a(t) \right. \\ &+ \left. \left. \sqrt{\mathcal{L}_{CT_b} \mathcal{L}_{T_bR}} |h_{CT_b} h_{T_bR}| e^{-j\phi_b} x_b(t) \right) \right] e^{-j2\pi\Delta F t} \\ &+ n(t). \end{aligned} \quad (2.7)$$

Notice that the term inside the brackets of Eq. (2.7) consists of a complex, time-

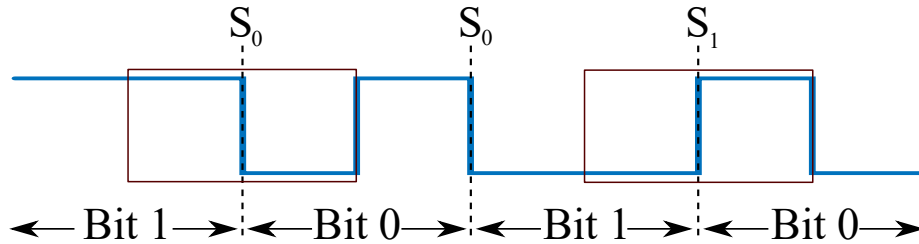


Figure 2.1: FM0 line-coded waveform of a single RFID tag.

independent DC offset plus two tag/time-dependent terms.

Due to the fact that the receiver and the emitter share the same local oscillator on the SDR device,  $\Delta F = \Delta\phi = 0$  are assumed zero in the monostatic case. It is further assumed that the receiver/reader can estimate and remove the DC offset, Eq. (2.7) (with the help of Eq. (2.2)) is simplified to the following DC-blocked received signal during bit period  $T$ :

$$\tilde{y}(t) = h_a \mu_a x_a(t) + h_b \mu_b x_b(t) + n(t), \quad (2.8)$$

where parameter  $\mu_m$  incorporates the compound scatter radio link path-losses and tag-related parameters,

$$\mu_m = \sqrt{2\eta P_c} L_{\text{TmR}} (\Gamma_0 - \Gamma_1), \quad m \in \{a, b\}, \quad (2.9)$$

and  $n(t)$  stands for the additive thermal noise at the receiver, modelled by a complex, circularly symmetric, additive Gaussian noise process with the following power spectral density:

$$S_{nn}(F) = \begin{cases} \frac{N_0}{2}, & |F| \leq W \\ 0, & \text{otherwise} \end{cases}, \quad (2.10)$$

where  $W$  stands for receiver's bandwidth.<sup>1</sup>

### 2.1.3 FM0 Line Coding

Nominal bit duration is denoted by  $T$  and sampling period by  $T_s$ ; oversampling factor  $L \triangleq \frac{T}{T_s}$  (not to be confused with path-loss model  $L_k$ ) is assumed, without loss of generality, to be an even number. An example of FM0 line coding is shown Fig. 2.1;

<sup>1</sup> $N_0 = k_b T_\theta$ , where  $k_b$  and  $T_\theta$  are the Boltzmann constant and receiver temperature, respectively

notice that the line always changes level at bit boundaries and at the middle of bit '0'. After shifted examination of the transmitted waveform by  $T/2$  before the beginning of the bit for a single user/tag FM0 and observing signal of duration  $T$ , only one of the following waveforms can be observed,  $S_0(t), S_1(t)$  (instead of four), marked in Fig. 2.1 with rectangles:

$$S_0(t) = \begin{cases} 1, & \text{if } 0 \leq t < \frac{T}{2} \\ 0, & \text{if } \frac{T}{2} \leq t < T \end{cases}, S_1(t) = \begin{cases} 0, & \text{if } 0 \leq t < \frac{T}{2} \\ 1, & \text{if } \frac{T}{2} \leq t < T \end{cases}. \quad (2.11)$$

Taking into account the memory induced by FM0, ML sequence detection rule is simplified to observing  $2T$ -signal duration for each bit of duration  $T$  [41, 42]; assuming  $\hat{d} = 0$  ( $\hat{d} = 1$ ) if  $S_0(t)$  ( $S_1(t)$ ) is detected,<sup>2</sup> the final decision for the transmitted bits  $b$  is computed as follows:

$$\hat{b}(n) = \hat{d}(n-1) \oplus \hat{d}(n), \quad (2.12)$$

where  $\oplus$  is the xor operator,  $\hat{d}(-1) = 0$  and  $\hat{d}(n-1), \hat{d}(n)$  correspond to decisions for two consecutive time-shifted (by  $T/2$ ) FM0 waveforms of duration  $T$  each. In other words, observation and processing of  $2T$ -signal duration suffices for optimal ML sequence detection [41, 42] and thus, for FM0 there is no need to run the Viterbi algorithm in a single-tag scenario. Sampling the received signal  $\tilde{y}(t)$  every  $kT_s, k \in \mathbb{N}$ , offers  $\tilde{y}[k] \equiv \tilde{y}(kT_s)$ . The sampled waveform is then filtered using a square pulse  $\Pi[k]$  of length  $L/2$  as follows:

$$y_f[n] = \sum_{k=-\infty}^{\infty} \tilde{y}[k] \Pi[n-k]. \quad (2.13)$$

In sharp contrast to prior art, this work considers a non-zero time offset between the two tags  $\tau' \in \{0, T_s, 2T_s, \dots, T - T_s\}$ , rendering conventional detection techniques suboptimal. Equivalently, the asynchrony can be represented by number of samples  $\tau \in \{0, 1, 2, \dots, L-1\}$ , as depicted in Fig. 2.2.

---

<sup>2</sup> $S_0(t)$  corresponds to  $\mathbf{e}_0 = [1 \ 0]^T$  and  $S_1(t)$  corresponds to  $\mathbf{e}_1 = [0 \ 1]^T$ .

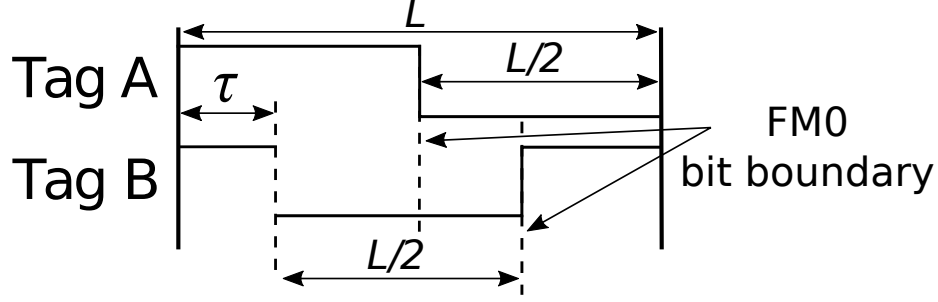


Figure 2.2: Tag  $a$  backscatters  $S_0(t)$  that corresponds to  $\mathbf{x}_{a,i} = \mathbf{e}_0$ . Tag  $b$  backscatters  $S_1(t)$ , delayed by  $\tau$  samples, corresponding to  $\mathbf{x}_{b,i} = \mathbf{e}_1$ . Immediately before that, tag  $b$  backscatters  $S_1(t)$ , which corresponds to  $\mathbf{x}_{b,i-1} = \mathbf{e}_1$ .

## 2.2 Problem Transformation

Fig. 2.2 depicts shifted by  $T/2$  observation of tag  $a$  signal, where  $S_0(t)$  is backscattered, while tag  $b$  backscatters waveform  $S_1(t)$ , preceded by  $S_1(t)$ , with a delay of  $\tau < L/2$  samples. The following theorem puts forth asynchronous detection, simplifying the problem in a compact way:

**Theorem 1.** *Assuming perfect symbol synchronization w.r.t. tag  $a$  and shifted by  $T/2$  observation (as in Fig. 2.2), the asynchronous, baseband equivalent model (after pulse matched filtering), including information  $\mathbf{x}_{a,i}$ ,  $\mathbf{x}_{b,i}$  from tag  $a$  and  $b$ , respectively, during the  $i$ -th FM0 symbol, as well as tag's  $b$  previous information symbol  $\mathbf{x}_{b,i-1}$ , is given as follows:*

$$\mathbf{y}_i = h_a \sqrt{\frac{\mathcal{E}_{bit}^a}{\mathbb{E}[|h_a|^2]}} \mathbf{x}_{a,i} + \mathbf{B}_{(i-1,i)} h_b \sqrt{\frac{\mathcal{E}_{bit}^b}{\mathbb{E}[|h_b|^2]}} \mathbf{x}_{b,i} + \mathbf{n}_i, \quad (2.14)$$

where  $\mathbf{n}_i \sim \mathcal{CN}(\mathbf{0}_2, \underbrace{N_0 W T_s}_{\sigma^2} \mathbf{I}_2) \equiv \mathcal{CN}(\mathbf{0}_2, \sigma^2 \mathbf{I}_2)$ ,  $\mathbf{x}_{a,i}$ ,  $\mathbf{x}_{b,i} \in \{\mathbf{e}_0, \mathbf{e}_1\}$ , with

$$\mathbf{e}_0 \triangleq \begin{bmatrix} 1 \\ 0 \end{bmatrix}, \quad \mathbf{e}_1 \triangleq \begin{bmatrix} 0 \\ 1 \end{bmatrix}, \quad (2.15)$$

and shaping matrix  $\mathbf{B}_{(i-1,i)} \in \mathbb{R}^{2 \times 2}$ , detailed in Table 2.1, is a function of  $\mathbf{x}_{b,i}$ ,  $\mathbf{x}_{b,i-1}$  and  $\tau \in \{0, 1, \dots, L-1\}$ :

$$\mathbf{B}_{(i-1,i)} \equiv \mathbf{B}(\tau, \mathbf{x}_{b,i-1}, \mathbf{x}_{b,i}).$$

Table 2.1: Shaping matrices  $\mathbf{B}_{(i-1,i)}$ .

$\tau < L/2$		
	$\mathbf{x}_{b,i} = [1 \ 0]^T$	$\mathbf{x}_{b,i} = [0 \ 1]^T$
$\mathbf{x}_{b,i-1} = \begin{bmatrix} 1 \\ 0 \end{bmatrix}$	$\mathbf{B}_1 = \begin{bmatrix} 1 - \frac{2\tau}{L} & 0 \\ \frac{2\tau}{L} & 0 \end{bmatrix}$	$\mathbf{B}_2 = \begin{bmatrix} 0 & 0 \\ 0 & 1 - \frac{2\tau}{L} \end{bmatrix}$
$\mathbf{x}_{b,i-1} = \begin{bmatrix} 0 \\ 1 \end{bmatrix}$	$\mathbf{B}_3 = \begin{bmatrix} 1 & 0 \\ \frac{2\tau}{L} & 0 \end{bmatrix}$	$\mathbf{B}_4 = \begin{bmatrix} 0 & \frac{2\tau}{L} \\ 0 & 1 - \frac{2\tau}{L} \end{bmatrix}$
$\tau \geq L/2$		
$\mathbf{x}_{b,i-1} = \begin{bmatrix} 1 \\ 0 \end{bmatrix}$	$\mathbf{B}_1 = \begin{bmatrix} \frac{2\tau}{L} - 1 & 0 \\ 2 - \frac{2\tau}{L} & 0 \end{bmatrix}$	$\mathbf{B}_2 = \begin{bmatrix} 0 & \frac{2\tau}{L} - 1 \\ 0 & 0 \end{bmatrix}$
$\mathbf{x}_{b,i-1} = \begin{bmatrix} 0 \\ 1 \end{bmatrix}$	$\mathbf{B}_3 = \begin{bmatrix} 2 - \frac{2\tau}{L} & 0 \\ 1 & 0 \end{bmatrix}$	$\mathbf{B}_4 = \begin{bmatrix} 0 & 2 - \frac{2\tau}{L} \\ 0 & \frac{2\tau}{L} - 1 \end{bmatrix}$

*Proof.* The proof is given in Appendix 7.1.1. ■

Table 2.1, offers the 8 possible different values for matrix  $\mathbf{B}_{(i-1,i)}$ . The rows of the matrix correspond to the first and the second half-bits,  $y_0^i$  and  $y_1^i$ , respectively. More specifically the row values of the matrix encompass the part of the detection window, where signal from tag  $b$  is present. The columns of the matrix correspond to tag  $b$  emitting  $\mathbf{x}_{b,i} = [1 \ 0]^T$  or  $\mathbf{x}_{b,i} = [0 \ 1]^T$ , respectively. By definition, a signal like  $\mathbf{x}_{b,i} = [1 \ 1]^T$  can never be observed, therefore one column will always be filled with zeros. Table 2.2 encodes the possible (output) values of matrix  $\mathbf{B}_{(i-1,i)}$ , as a function of tag  $b$ 's consecutive information  $\mathbf{x}_{b,i-1}$ ,  $\mathbf{x}_{b,i}$ .

### 2.2.1 Number of Clusters

After processing a number of samples of the received signal as in Eq. (2.13) or Eq. (2.14), the number of clusters observed in the I/Q plane varies for different

Table 2.2: Transmitted symbol combinations.

$\mathbf{x}_{a,i}$	$\mathbf{e}_0$	$\mathbf{e}_1$	$\mathbf{e}_0$	$\mathbf{e}_1$	$\mathbf{e}_0$	$\mathbf{e}_1$	$\mathbf{e}_0$	$\mathbf{e}_1$
$\mathbf{x}_{b,i}$	$\mathbf{e}_0$	$\mathbf{e}_1$	$\mathbf{e}_1$	$\mathbf{e}_0$	$\mathbf{e}_0$	$\mathbf{e}_1$	$\mathbf{e}_1$	$\mathbf{e}_0$
$\mathbf{x}_{b,i-1}$	$\mathbf{e}_0$	$\mathbf{e}_0$	$\mathbf{e}_0$	$\mathbf{e}_0$	$\mathbf{e}_1$	$\mathbf{e}_1$	$\mathbf{e}_1$	$\mathbf{e}_1$
$\mathbf{B}_{(i-1,i)}$	$\mathbf{B}_1$	$\mathbf{B}_2$	$\mathbf{B}_2$	$\mathbf{B}_1$	$\mathbf{B}_3$	$\mathbf{B}_4$	$\mathbf{B}_4$	$\mathbf{B}_3$

values of  $\tau$ . More specifically, 4 clusters are produced for  $\tau \in \{0, \frac{L}{2}\}$ , 6 clusters are produced for  $\tau \in \{\frac{L}{4}, \frac{3L}{4}\}$ , while 8 clusters are produced for the remaining values  $\tau \in \{0, \dots, L-1\} / \{0, \frac{L}{4}, \frac{L}{2}, \frac{3L}{4}\}$ , after plotting the  $y_f$  samples every  $k\frac{L}{2}$ ,  $k \in \mathbb{N}$ , as in Fig. 1.1.<sup>3</sup> Even though no clustering methods are utilized in this work, this observation highlights the need for asynchrony consideration when utilizing clustering methods, e.g., depending on the processing followed of the received samples, 8 clusters may correspond to 2 (asynchronous) tags with some time offset or 3 tags in perfect synchrony.

### 2.2.2 SNR Calculation

Due to  $\tau \neq 0$ , it is shown below that the signal energy ratio between the two tags depends on that time offset parameter. The following definition is first presented:

**Definition 1.** Based on Eq. (2.8), the average received energy per bit for tag  $m$ , assuming FMO encoding observed with a  $T/2$  shift, is given by:

$$\mathcal{E}_{bit}^m \triangleq \mathbb{E} \left[ \mu_m^2 |h_m|^2 \int_0^T |x_m(t)|^2 dt \right] = \mu_m^2 \mathbb{E}[|h_m|^2] \frac{T}{2}. \quad (2.16)$$

The following lemma is given for tag signal-to-noise ratio (SNR):

**Lemma 1.** Based on Eqs. (2.14), (2.16), signal-to-noise ratio for tag  $a$  is given by:

$$\text{SNR}_a \triangleq \frac{\mathbb{E} \left[ \left| h_a \sqrt{\frac{\mathcal{E}_{bit}^a}{\mathbb{E}[|h_a|^2]}} \mathbf{x}_{a,i} \right|^2 \right]}{\mathbb{E}[|\mathbf{n}_i|^2]} = \frac{\mathcal{E}_{bit}^a}{2N_0WT_s}. \quad (2.17)$$

<sup>3</sup>Sampling of  $y_f[\cdot]$  every  $k\frac{L}{2}$ ,  $k \in \mathbb{N}$ , offers exactly the values of Eq. (2.14),  $\mathbf{y}_i$ , according to its derivation in Appendix 7.1.1.

*Proof.* The numerator stems from straightforward calculation and the fact that  $|\mathbf{x}_{a,i}| = |\mathbf{e}_0| = |\mathbf{e}_1| = 1$ ; the denominator calculation stems from Eq. (7.6). ■

Similarly, SNR for tag  $b$  follows:

**Lemma 2.** *Based on Eqs. (2.14), (2.16), tag  $b$  signal-to-noise ratio is given by:*

$$\begin{aligned} SNR_b &\triangleq \frac{\mathbb{E} \left[ \left| \mathbf{B}_{(i-1,i)} h_b \sqrt{\frac{\mathcal{E}_{bit}^b}{\mathbb{E}[|h_b|^2]}} \mathbf{x}_{b,i} \right|^2 \right]}{\mathbb{E}[|\mathbf{n}_i|^2]} \\ &= \begin{cases} \frac{\mathcal{E}_{bit}^b}{2N_0WT_s}, & \text{if } \tau = 0, \\ \frac{(5L^2 - 12L\tau + 12\tau^2) \mathcal{E}_{bit}^b}{4N_0WT_sL^2}, & \text{if } \tau > 0. \end{cases} \end{aligned} \quad (2.18)$$

*Proof.* For  $\tau = 0$  the proof stems from Lemma 1. For  $\tau > 0$  the proof is given in Appendix 7.1.2. ■

The following power ratio will be also found useful in the numerical results; as in every multi-user setup, performance is dictated not only by SNR, but also relative power among users/tags:

**Definition 2.** *The power ratio of tag  $a$  over  $b$  is defined as:*

$$PR_{ab} \triangleq \frac{SNR_a}{SNR_b}. \quad (2.19)$$

Finally, the following calculation will be needed in the link budget calculations and numerical results:

**Lemma 3.** *The 4-th moment of the Rician distribution is given by,*

$$\mathbb{E}[|h_m|^2] \triangleq \mathbb{E}[|h_{T_mR}|^4] = \frac{(\sigma_{h_{T_mR}}^2)^2 (\kappa_m^2 + 4\kappa_m + 2)}{(\kappa_m + 1)^2}. \quad (2.20)$$

*Proof.* The proof is given in Appendix 7.1.3. ■

## 2.3 Detection Techniques

This work exploits the transformation of Section 2.2 and processes the signal with a  $T/2$  time-shift. Depending on the duration of the signal observed before

detection, there are several detectors that can be tested, described below;  $\hat{h}_m$  stands for  $h_m \sqrt{\frac{\mathcal{E}_{bit}^m}{\mathbb{E}[|h_m|^2]}}$  for tag  $m \in \{a, b\}$ , which is either estimated or perfectly known;  $\tau$  is assumed known through estimation; algorithms that estimate these parameters are offered next, in Section 2.4.

### 2.3.1 $T$ Detection for Tag $b$

In the case of tag  $b$  detection, the detector that minimizes bit error rate (BER) of the received signal, utilizing a  $T$ -signal duration, is given by the minimum distance rule:

$$\hat{\mathbf{x}}_{a,i}, \hat{\mathbf{x}}_{b,i}, \hat{\mathbf{x}}_{b,i-1} = \underset{\substack{\mathbf{x}_{a,i}, \\ \mathbf{x}_{b,i}, \mathbf{x}_{b,i-1}}}{\text{argmin}} \left\{ \|\mathbf{y}_i - \hat{h}_a \mathbf{x}_{a,i} - \mathbf{B}_{(i-1,i)} \hat{h}_b \mathbf{x}_{b,i}\|_2^2 \right\}, \quad (2.21)$$

From Eq. (2.21), only bit information of tag  $b$  can be detected, through  $\hat{\mathbf{x}}_{b,i}$  and  $\hat{\mathbf{x}}_{b,i-1}$  and Eq. (2.12). However, this method is suboptimal since it does not utilize a  $2T$  detection window, required for BER-optimal FM0 decoding.

### 2.3.2 $2T$ Detection for Tag $a$

In the case of  $2T$  tag  $a$  detection, the first  $T$ -block is used to detect  $\hat{\mathbf{x}}_{a,i-1}$  and the second  $T$ -block is used to detect  $\hat{\mathbf{x}}_{a,i}$ ; information from tag  $b$  is not detected jointly across the two consecutive  $T$ -blocks:

$$\begin{aligned} \hat{\mathbf{x}}_{a,i}, \hat{\mathbf{x}}_{a,i-1} = \underset{\substack{\mathbf{x}_{a,i}, \mathbf{x}_{a,i-1}, \\ \mathbf{x}_{b,i}, \mathbf{x}_{b,i-1}, \mathbf{x}'_{b,i-1}, \mathbf{x}_{b,i-2}}}{\text{argmin}} \left\{ \|\mathbf{y}_i - \hat{h}_a \mathbf{x}_{a,i} - \mathbf{B}_{(i-1,i)} \hat{h}_b \mathbf{x}_{b,i}\|_2^2 \right. \\ \left. + \|\mathbf{y}_{i-1} - \hat{h}_a \mathbf{x}_{a,i-1} - \mathbf{B}_{(i-2,i-1)} \hat{h}_b \mathbf{x}'_{b,i-1}\|_2^2 \right\}. \end{aligned} \quad (2.22)$$

Thereinafter,  $\hat{\mathbf{x}}_{a,i}, \hat{\mathbf{x}}_{a,i-1}$  are used according to Eq. (2.12) to detect the information bit. However, the above also gives  $\hat{\mathbf{x}}_{b,i-2}, \hat{\mathbf{x}}'_{b,i-1}$  from the first  $T$ -block and  $\hat{\mathbf{x}}_{b,i-1}, \hat{\mathbf{x}}_{b,i}$  from the second  $T$ -block. Considering that  $\hat{\mathbf{x}}'_{b,i-1} \neq \hat{\mathbf{x}}_{b,i-1}$  from one  $T$ -block to the other, this detector is suboptimal.

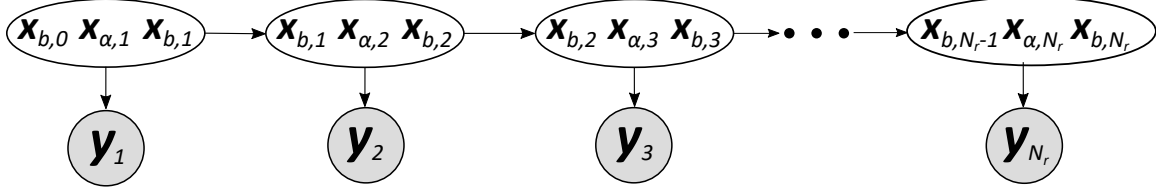


Figure 2.3: Hidden Markov Model of the proposed signal model.

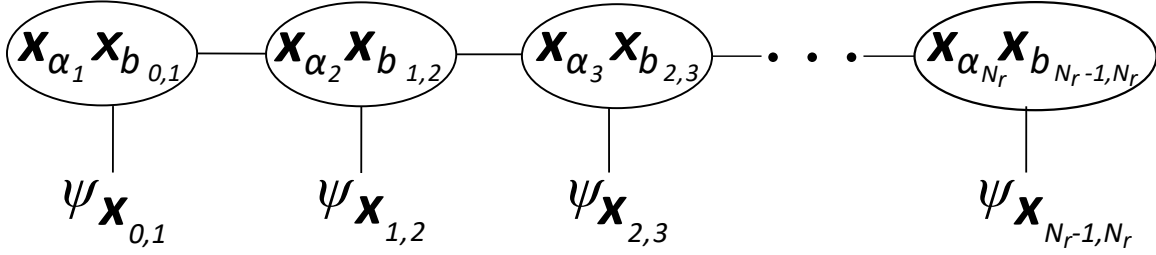


Figure 2.4: Truncated probabilistic graphical model.

### 2.3.3 $2T$ Detection for Tag $a$ and Tag $b$

In this case, both tags are jointly decoded using  $2T$  signal observation:

$$\hat{\mathbf{x}}_{a,i}, \hat{\mathbf{x}}_{a,i-1}, \hat{\mathbf{x}}_{b,i}, \hat{\mathbf{x}}_{b,i-1}, \hat{\mathbf{x}}_{b,i-2} = \underset{\substack{\mathbf{x}_{a,i}, \mathbf{x}_{a,i-1}, \\ \mathbf{x}_{b,i}, \mathbf{x}_{b,i-1}, \mathbf{x}_{b,i-2}}}{\text{argmin}} \left\{ \|\mathbf{y}_i - \hat{h}_a \mathbf{x}_{a,i} - \mathbf{B}_{(i-1,i)} \hat{h}_b \mathbf{x}_{b,i}\|_2^2 \right. \\ \left. + \|\mathbf{y}_{i-1} - \hat{h}_a \mathbf{x}_{a,i-1} - \mathbf{B}_{(i-2,i-1)} \hat{h}_b \mathbf{x}_{b,i-1}\|_2^2 \right\}. \quad (2.23)$$

### 2.3.4 Viterbi

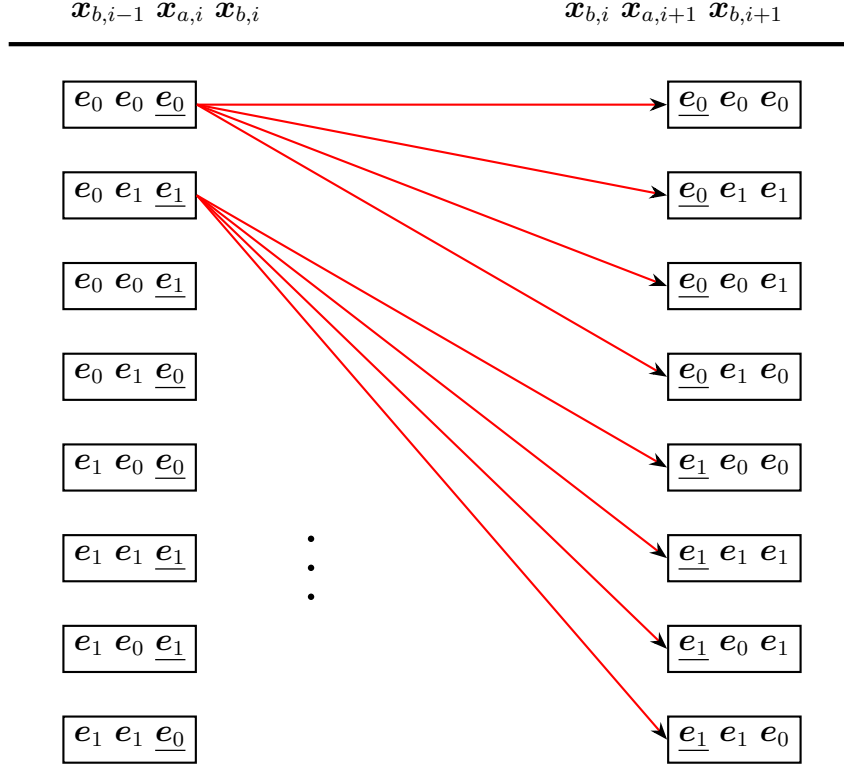
In the case of the Viterbi joint sequence detection, the proposed system model can be represented by the hidden Markov model (HMM) of Fig. 2.3, where the shaded and white nodes represent the observed random variables and the hidden states, respectively, [43]. Incorporating the observed data into the HMM, the truncated HMM of Fig. 2.4 is obtained, where  $\psi_{\mathbf{x}_{a_i} \mathbf{x}_{b_{i-1,i}}, \mathbf{y}_i} \triangleq \psi_{\mathbf{x}_{i-1,i}}$  denotes the resulting singleton potentials. To further ease notation,  $\mathbf{x}_{b,i-1} \mathbf{x}_{b,i} \triangleq \mathbf{x}_{b_{i-1,i}}$ .

The transition probabilities are defined as follows:

$$\mathbb{P}(\mathbf{x}_{a_2} = \mathbf{a}, \mathbf{x}_{b_{1,2}} = \mathbf{cd} | \mathbf{x}_{b_1} = \mathbf{b}) \triangleq \mathbb{1}(\mathbf{b} = \mathbf{c}), \quad (2.24)$$

$$\mathbb{P}(\mathbf{x}_{a_{i+1}} = \mathbf{a}, \mathbf{x}_{b_{i,i+1}} = \mathbf{df} | \mathbf{x}_{b_{i-1,i}} = \mathbf{bc}) \triangleq \mathbb{1}(\mathbf{c} = \mathbf{d}), \quad (2.25)$$

where  $\mathbf{a}, \mathbf{b}, \mathbf{c}, \mathbf{d}, \mathbf{f}, \mathbf{g} \in \{\mathbf{e}_0, \mathbf{e}_1\}$ ,  $\mathbf{x}_{b_{i,i+1}} = \mathbf{cd}$  stands for  $\mathbf{x}_{b,i} = \mathbf{c}$ ,  $\mathbf{x}_{b,i+1} = \mathbf{d}$  and

Figure 2.5: Stages  $i$  and  $i + 1$  of the Viterbi trellis diagram.

$i \in \{1, 2, \dots, N_r - 1\}$  with  $N_r = 16$  denoting the number of bits in the RN16 packet. The above states that the allowed transitions are those where  $\mathbf{x}_{b,i}$  of stage  $i$  is the same as  $\mathbf{x}_{b,i}$  of stage  $i + 1$ , as in Fig. 2.5.

The singleton potential functions are given by:

$$\psi_{\mathbf{x}_{i-1,i}}(\mathbf{a}, \mathbf{bc}) \propto \exp \left\{ -\frac{\|\mathbf{y}_i - \hat{h}_a \mathbf{x}_{a,i} - \mathbf{B}_{(i-1,i)} \hat{h}_b \mathbf{x}_{b,i}\|_2^2}{\sigma^2} \right\}, \quad (2.26)$$

where  $\psi_{\mathbf{x}_{i-1,i}}(\mathbf{a}, \mathbf{bc}) = \psi(\mathbf{x}_{a,i} = \mathbf{a}, \mathbf{x}_{b_{i-1,i}} = \mathbf{cd}, \mathbf{y}_i)$  and  $\mathbf{x}_{b_{i-1,i}}$  is encoded into the shaping matrix  $\mathbf{B}_{(i-1,i)}$ . In Eq. (2.26), for  $i = 1$ ,  $\mathbf{x}_{b,i-1} = \mathbf{x}_{b,0} = [1 \ 0]^T$ , where 1 is the last bit of the preamble sequence and 0 is the first bit of the FM0 line-coded RN16 sequence.

Since  $\mathbb{P}(\mathbf{x}_{a,i+1} = \mathbf{a}, \mathbf{x}_{b_{i,i+1}} = \mathbf{df} | \mathbf{x}_{b_{i-1,i}} = \mathbf{bc}) = \mathbb{1}(\mathbf{c} = \mathbf{d})$ , taking its logarithm results to either 0 or  $-\infty$  and hence, we omit it in the following process but also keep in mind only the legal transitions. Using the Max-Sum message update equation the

following is obtained:

$$\begin{aligned}
\log m_{(i-1,i) \rightarrow (i,i+1)}(\mathbf{a}, \mathbf{df}) &= \max_{\mathbf{g}, \mathbf{b}} \left\{ \log \psi_{\mathbf{x}_{i-1,i}}(\mathbf{g}, \mathbf{bd}) + \log m_{(i-2,i-1) \rightarrow (i-1,i)}(\mathbf{g}, \mathbf{bd}) \right\} \\
&= \max_{\mathbf{g}, \mathbf{b}} \left\{ -\|\mathbf{y}_i - \hat{h}_a \mathbf{x}_{a,i} - \mathbf{B}_{(i-1,i)} \hat{h}_b \mathbf{x}_{b,i}\|_2^2 \right. \\
&\quad \left. + \log m_{(i-2,i-1) \rightarrow (i-1,i)}(\mathbf{g}, \mathbf{bd}) \right\}, \tag{2.27}
\end{aligned}$$

where  $\mathbf{x}_{a,i+1} = \mathbf{a}$ ,  $\mathbf{x}_{a,i} = \mathbf{g}$ ,  $\mathbf{x}_{b,i+1} = \mathbf{f}$ ,  $\mathbf{x}_{b,i} = \mathbf{d}$  and  $\mathbf{x}_{b,i-1} = \mathbf{b}$ .

In the forward pass of the Viterbi algorithm, the edge weights are calculated for each stage of the probabilistic graphical model (Figs. 2.4, 2.5), according to Eq. (2.27), while also keeping track of the node with the optimal weight, necessary for the backtracking process. In the backward pass of the algorithm, the path that sums to the optimal total weight is obtained, offering the optimal FM0 transmitted sequence both for tag  $a$  and tag  $b$ . The above setup can be visualized using the trellis diagram of Fig. 2.5. Complexity of the Viterbi algorithm for a hidden Markov model (HMM) of a sequence of  $N$  hidden variables, each assuming  $|X|$  discrete values, is given by  $O(N|X|^2)$ . Thus, the complexity of the joint sequence detection through Viterbi is given by  $O(N(2^3)^2) = O(64 N)$ , according to Figs. 2.3, 2.4;  $N$  corresponds to the number of RN16 bits, and thus,  $N = 16$ .

### 2.3.5 Zero-Forcing

The single antenna zero-forcing (ZF) detector proposed in [5], treats one of the two tag responses as interference and projects the signal constellation into the subspace that completely cancels the interference, orthogonal to the interfering component:

$$\mathbf{s}_a[k] = \left[ \mathbf{I}_2 - \frac{\mathbf{h}_b \mathbf{h}_b^T}{\mathbf{h}_b^T \mathbf{h}_b} \right] \mathbf{s}[k], \tag{2.28}$$

$$\mathbf{s}_b[k] = \left[ \mathbf{I}_2 - \frac{\mathbf{h}_a \mathbf{h}_a^T}{\mathbf{h}_a^T \mathbf{h}_a} \right] \mathbf{s}[k], \tag{2.29}$$

where  $\mathbf{h}_a = [\Re\{\hat{h}_a\} \Im\{\hat{h}_a\}]^T$ ,  $\mathbf{h}_b = [\Re\{\hat{h}_b\} \Im\{\hat{h}_b\}]^T$ ,  $\mathbf{s}[k] = [\Re\{y_f[k]\} \Im\{y_f[k]\}]^T$  and  $y_f[k]$  is according to Eq. (2.13). The projection  $\mathbf{s}_m$  of each tag signal is thereafter decoded separately. This receiver is capable of resolving a collision from *strictly* two tags participating, since a subspace cannot be found in the two-dimensional I/Q plane, which is orthogonal to more than one interferer.

## 2.4 Digital Link Housekeeping

### 2.4.1 DC Estimation

In Gen2 applications, the DC offset is estimated by averaging the received samples acquired from the signal part right after the `QUERY` command has been sent from the reader, up to the point before the tags start switching, defined as interval  $T_1$  [1]. The estimated offset is then subtracted from each sample of Eq. (2.7), offering Eq. (2.8).

### 2.4.2 Channel Estimation

The algorithm used to estimate the channel coefficients follows work in [4]. In order to obtain the channel estimates, the received samples are projected onto the subspace defined by the DC component and the  $h_a + h_b$  cluster. The  $\widehat{h_a + h_b}$  estimate can be obtained either from the end or from the start of the preamble packet, defined as  $\mathbf{s}_p = [1 \ 1 \ 0 \ 1 \ 0 \ 0 \ 1 \ 0 \ 0 \ 0 \ 1 \ 1]$  in [1], for a single tag. At these positions there are two consecutive data-1 bits, so even after the observed shifting due to the delayed response of tag  $b$ , the upsampled (by  $L$ ) superimposed sequences will still have overlapping data-1 bits, offering an estimate for  $h_a + h_b$ .

The algorithm is based on the observation that two states (out of the possible 4, 6 or 8, see Sec. 2.2.1), are realized during the transmission of the RN16 packet preamble (due to common information transmission from the two tags, assuming synchrony), defining an one-dimensional subspace  $s_x$  (i.e., a line). Projecting the received samples of the RN16 packet onto the subspace orthogonal to  $s_x$ , will give a non-zero value if the corresponding half-bit is equal to  $h_a$  or  $h_b$ . The algorithm searches for points that have the maximum signal strength in this orthogonal subspace. More specifically, the received waveform is processed with matched filtering, offering  $y_f$ , and the maximum signal strength indices and corresponding channel coefficients, are estimated as follows:

$$k_A = \operatorname{argmax}_{k \in \{0, \dots, NL\}} \Im \left\{ y_f[k] e^{-j/\widehat{h_a + h_b}} \right\}, \quad (2.30)$$

$$k_B = \operatorname{argmin}_{k \in \{0, \dots, NL\}} \Im \left\{ y_f[k] e^{-j/\widehat{h_a + h_b}} \right\}, \quad (2.31)$$

$$\hat{h}_a = y_f[k_A], \quad (2.32)$$

$$\hat{h}_b = y_f[k_B], \quad (2.33)$$

where  $\mathbf{N} = \mathbf{N}_p + \mathbf{N}_r$  is the total number of transmitted bits (preamble + RN16). It is important to ensure that the estimates  $\hat{h}_a$  and  $\hat{h}_b$  are correctly assigned to each tag or if they need to be swapped, otherwise the performance of the detection methods will not be optimal. In order to check that  $\hat{h}_a$  indeed corresponds to tag  $a$  and  $\hat{h}_b$  to tag  $b$ , a mean squared error metric is utilized in this work, detailed in Sec. 2.4.3, below.

Even though this algorithm was initially developed for values of  $\tau < L/10$ , it still works in this problem formulation, as will be shown in the numerical results section; that is due to the fact that the projection of all samples will always be closer to the subspace  $s_x$  than the samples corresponding to  $h_a$  and  $h_b$ , no matter the value of  $\tau$  or the number of clusters it produces on the I/Q plane.

### 2.4.3 Time Offset Estimation

Time offset  $\tau$  estimation is based on channel state information (CSI) estimation. By the problem's definition tag  $a$  responds first ( $\tau_a = 0$ ); thus, the detected packet start of the collided RN16 sequence, is also the start of tag  $a$  response. In order to detect the RN16 packet start, a correlation-based method is utilized with the (known) preamble bits of RN16. The time offset estimation algorithm is based upon creating the discrete channel equivalent, which basically is an ideal superposition of the two tags preamble bits sequences for different values of  $\tau$  and comparing it, using the minimum distance rule, to the received samples of the preamble part of the packet. An estimate for  $\tau$  is thus obtained by minimizing the following mean squared error (MSE):

$$\hat{\tau} = \underset{\tau \in \{0,1,\dots,L-1\}}{\operatorname{argmin}} \frac{1}{K} \sum_{k=0}^{K-1} |y_f[k] - c_f[k]|^2, \quad (2.34)$$

where  $K = \mathbf{N}_p L$ ,  $\mathbf{N}_p = 6$  the number of preamble bits and  $c_f[k]$  the output of the matched filtering process, with a square pulse  $\Pi[k]$  of length  $L/2$ , on the discrete channel equivalent  $c[k]$ ; the latter is defined as follows:

$$c[k] = \hat{h}_a \mathbf{s}_{p,\text{up}} + \hat{h}_b \underbrace{[0 \dots 0]_{\tau}}_0 \mathbf{s}_{p,\text{up}}, \quad (2.35)$$

$$c_f[n] = \sum_{k=-\infty}^{\infty} c[k] \Pi[n - k], \quad (2.36)$$

---

where  $\mathbf{s}_{p,\text{up}}$  denotes the upsampled, by a factor of  $L$ , preamble bits sequence. Notice that  $c_f[n]$  above requires estimates of the channels  $\hat{h}_a, \hat{h}_b$ .

In order to check whether the channel estimates are correctly assigned to each tag, the above time offset algorithm must be run twice, once with  $\hat{h}_a$  corresponding to tag  $a$  and  $\hat{h}_b$  to tag  $b$  and once more where the mapping is *swapped*. The channel estimates are then accordingly mapped, depending on which of the two runs returned the minimum MSE.

# Chapter 3

## Simulation & Experimental Evaluation of Asynchronous Reception

In this chapter, performance evaluation of the detection schemes proposed in Chapter 2, is conducted via simulations on MATLAB, as well as with experimental data, using commodity Gen2 RFID tags and implementation of the proposed scheme in C++ and software-defined radio.

### 3.1 Simulation Results

Figs. 3.1, 3.2, 3.3 are offered with  $10^4$  Monte Carlo runs per SNR value, while channel parameters remained constant for each run. The rest of the parameters follow:  $N_p = 6$  preamble and  $N_r = 16$  payload bits,  $f_c = 868$  MHz, BLF = 40 kHz,  $F_s \triangleq 1/T_s = 2$  MHz,  $L = T/T_s \equiv F_s/\text{BLF} = 50$ ,  $T = 1/\text{BLF} = 25 \mu\text{s}$ ,  $\kappa_a = 10$ ,  $\kappa_b = 9$ ,  $v_a = v_b = 4$ ,  $\Gamma_0 = 0$ ,  $\Gamma_1 = 1$ ,  $\eta = 10\%$  and  $P_c$  ranging from 15 to 30 dBm. Different operating regimes of the detectors are evaluated, since the tag-to-reader distances are altered from  $d_a = 7.5$  m and  $d_b = 8.0$  m in Fig. 3.1, to  $d_a = 8.5$  m and  $d_b = 7.6$  m in Fig. 3.3, offering different tag power ratio ( $\text{PR}_{ab}$  or  $\text{PR}_{ba}$  according to Eq. (2.19)). Results will be presented assuming perfect CSI and  $\tau$  estimation (ideal case), as well as estimated CSI and  $\tau$  (practical case), according to the algorithms presented in Sec. 2.4.

Fig. 3.1a depicts the synchronous collision case, i.e.,  $\tau = 0$ , where the  $2T$  detectors (Sec. 2.3.2, 2.3.3) offer, as expected, the exact same performance with the Viterbi joint detector; FM0 induced memory within two symbol periods is adequate for detection [42] and thus, longer memory - exploited in Viterbi - is not needed. However, detectors' performance does not coincide in the asynchronous case, in Figs. 3.1b, 3.1c, where  $\tau = 10$ ,  $\tau = 25$ , respectively. The performance gap of the  $2T$  detectors com-

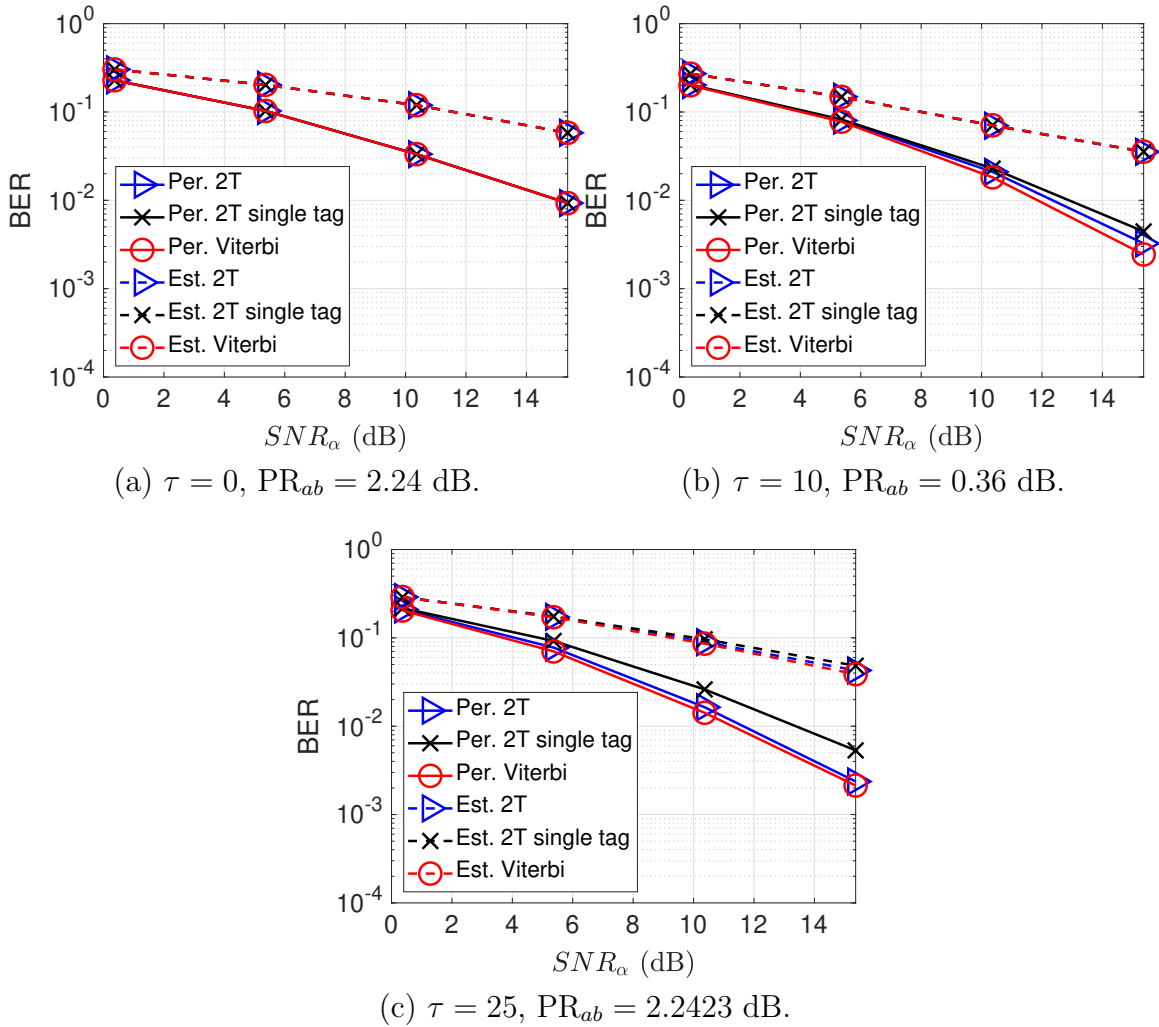


Figure 3.1: Tag  $a$  BER evaluation at  $d_a = 7.5$  m,  $d_b = 8.0$  m.

pared to Viterbi in the asynchronous case is due to the extra induced memory from the delayed tag  $b$ ; such delay requires detection of information from additional symbols (compared to the synchronous case), rendering the  $2T$  detectors suboptimal. In the asynchronous case, the  $2T$  detection of both tags outperforms the  $2T$  detection of (single) tag  $a$  only, as expected. At the high SNR regime, in the order of 15 dB, offered BER with estimated (perfect) channel is in the order of 3% (0.4%) and thus, the expected number of erroneously detected RN16 bits is strictly less than 1. The latter clearly shows that RN16 tag collision is not an issue for the specific detectors. Moreover, the value of  $\tau$  in the detectors' performance is important and presents an oscillating behaviour; BER is not monotonically increasing (or decreasing) as a function of  $\tau$ .

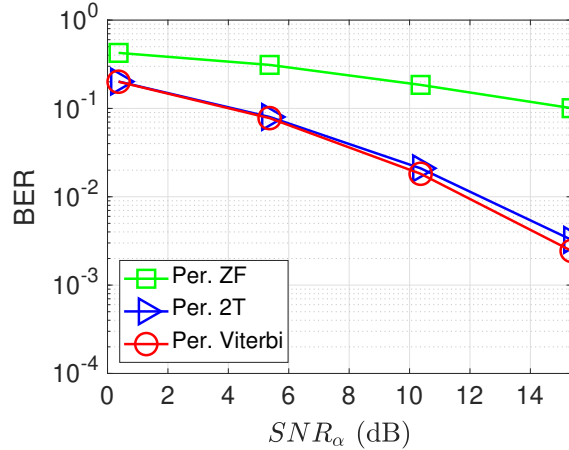
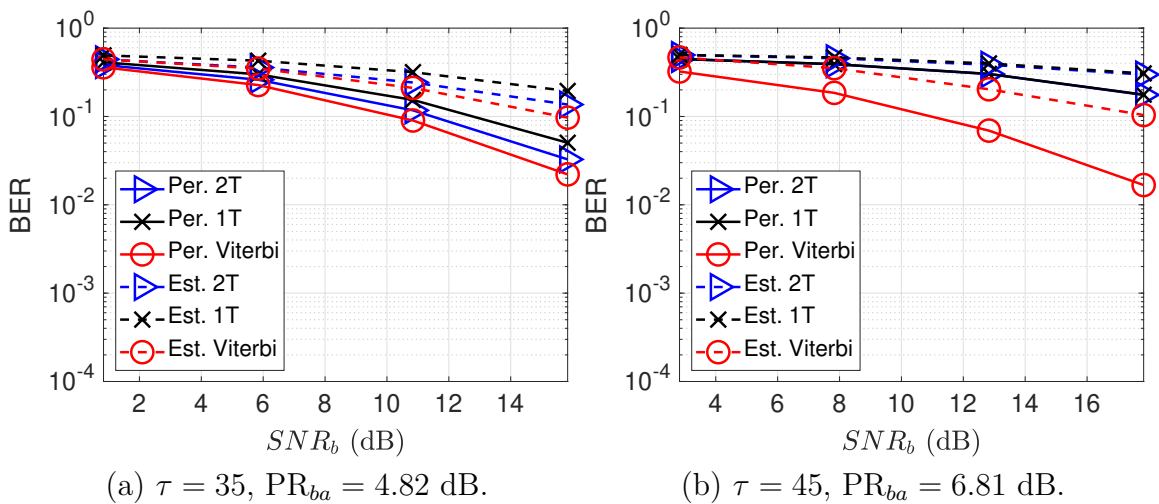
Figure 3.2: Tag  $a$  BER evaluation at  $\tau = 10$ .Figure 3.3: Tag  $b$  BER evaluation at  $d_a = 8.5$  m,  $d_b = 7.6$  m.

Fig. 3.2 compares performance of the zero-forcing, the joint  $2T$  and the Viterbi detector for tag  $a$ , under perfect CSI, with the same simulation parameters as Fig. 3.1b. It can be clearly observed that both  $2T$  and the Viterbi detector outperform the ZF detector; that is expected since the latter does not initially take into account asynchrony, i.e., the time offset between the two tags, before the projection is performed. Thus, it is important to employ detection techniques that explicitly take into account asynchronous operation of tags, which is not uncommon in commercial RFID systems.

Figs. 3.3a, 3.3b demonstrate the performance of the  $1T$ , joint  $2T$  and the Viterbi detectors for tag  $b$  data detection in the asynchronous case, where  $\tau = 35$  and  $\tau = 45$ , respectively, when tag  $b$  signal is stronger than tag  $a$ . The oscillating BER behaviour

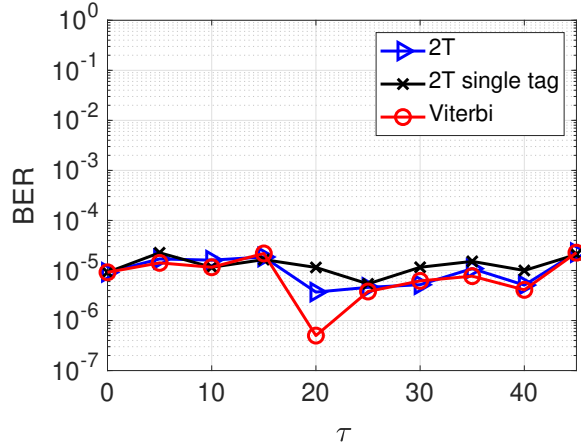


Figure 3.4: Delay offset impact on BER of tag  $a$ .

of Fig. 3.1 is once again observed in both Figs. 3.3a, 3.3b, while the performance gap between Viterbi and the  $1T$ , joint  $2T$  detectors is clearly more notable in Fig. 3.3b, for  $\tau = 45$ . At the high SNR regime around 16 dB, BER with estimated (perfect) channel is in the order of 10% (2%); 10% BER does not suffice for zero-error RN16 detection of tag  $b$ . Thus, it is important for the reader to flip the roles between tag  $a$  and  $b$ , and treat the stronger signal as tag  $a$ . However, that requires more research on packet synchronization techniques, that could lock to the stronger packet/tag, irrespectively of the delay among the two tags. It is noted that the literature typically offers packet synchronization techniques that lock on the packet that arrives first (e.g., work in [44]).

Fig. 3.4 demonstrates detection performance for different delay values, under estimated CSI. The parameters used in this simulation are as follows:  $P_c = 20$  dBm,  $d_a = d_b = 0.6$  m,  $f_c = 900$  MHz,  $F_s = 20$  MHz, BLF = 100 kHz,  $\eta = 0.1$ , and  $v_a = v_b = 2$ , while  $10^5$  Monte Carlo runs were conducted.<sup>1</sup> Under perfect CSI, the observed BER was found equal to BER = 0, while under estimated CSI, the observed BER was found less than  $10^{-4}$ , for any value of  $\tau$ . It is noted that under similar conditions, prior art algorithms in [14], offered BER in the order of BER  $\geq 10^{-4}$ .

<sup>1</sup>Decimation factor of 4 was also utilized, reducing to  $L = 50$  from nominal  $L = 200$ .

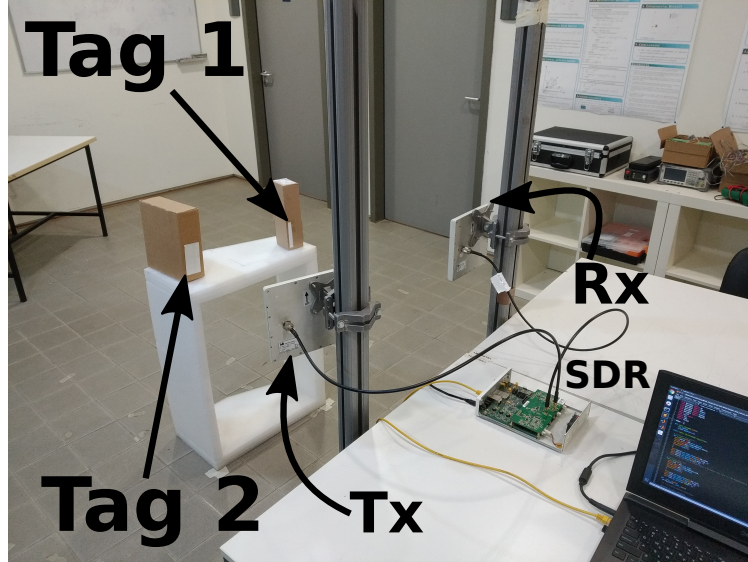


Figure 3.5: Experimental setup with SDR implementation of Gen2. The anti-collision algorithm was implemented in C++.

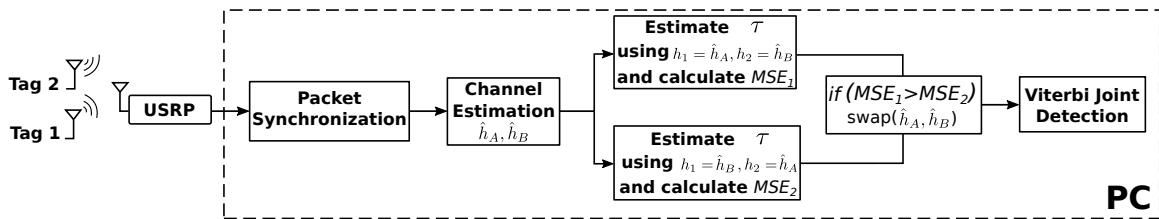


Figure 3.6: Block diagram of the collision resolution process.

Table 3.1: Experimental performance evaluation.

	Measured RSSI	Single Tag Detection	This work
80 cm	-9.5 dBm	28.55%	43.25%
130 cm	-11.9 dBm	25.80%	33.80%
280 cm (with Amplifier)	-15.8 dBm	25.30%	33.20%
300 cm (with Amplifier)	-14.5 dBm	11.85%	22.40%

## 3.2 Experimental Evaluation using Software-Defined Radio (SDR)

The algorithm was developed in C++ and integrated into the open-source Gen2 software stack developed in [2]. In all experiments, 2 Gen2 UHF RFID tags (1 ALN-9840-WRW and 1 ZEBRA 4"×2" Z-PERFORM 1500T) were attached to empty boxes, at various distances away for the reader antennas, as shown in Fig. 3.5. The

experimental setup included a USRP N200 with an RFX900 daughterboard and two circularly-polarized MTI MT-242032 antennas (one for Tx and one for Rx) with a gain of 7 dBic each. A spectrum analyzer was used to measure the received signal strength indicator (RSSI) at the location of the tags and at the carrier frequency of 868 MHz at which the whole system operated. A 24 dB Mini-Circuits ZRL-1200+ amplifier was also exploited in addition to a 9 dB attenuator between the amplifier and the RFX daughterboard. The software was executed in a laptop computer. Number of slots per round was set equal to 1, in order to force the collision. The total number of inventory rounds was set to 2000 in each experiment and various levels of distances and respective RSSI were tested. DC cancellation, channel estimation, time offset estimation and packet synchronization were implemented, as described in Section 2.4; the whole process followed is visualized at the block diagram of Fig. 3.6.

Since commercial RFID tags were used, their RN16 information is randomized and thus, not a-priori known. In order to make sure that the algorithm correctly detected RN16, the following approach was used: a tag will respond with its EPC information only if the reader acknowledges its correct RN16. Since, collision resolution is executed at the reader, correct acknowledge of tag RN16 information from the SDR reader will be followed by EPC transmission from a tag.

Table 3.1 shows the experimental results. For two tags placed 80 cm away from the reader antennas, the single tag detection algorithm offered successful tag interrogation around 560 times out of 2000 (corresponding to 28.55% success rate); in contrast, the collision resolution method of this work increased the successful interrogations to around 865 times out of 2000 (corresponding to 43.25% success rate). It is noted that single tag detection is utilized in SIC-based techniques, which are more appropriate for multi-user scenarios with significant differences among the users' received signal power. Performance gains around 10% were observed for other communication distances, with or without the amplifier. Such performance gains in the order of 10% increase the reading rate of any commercial RFID reader by that amount, without any hardware modifications and thus, may be of great commercial value. It was also observed during the experiments that the tags' RF energy harvesting and backscattering operation was affected in a non-linear way by distance and amplification gain, as expected; such behaviour will be further studied in future work.

---

### 3.3 Discussion

It was clearly shown that the proposed detectors leveraging the closed form signal model, demonstrated robust performance in a 2-tags collision scenario. It was demonstrated for the first time, that even though the performance gap between the joint  $2T$  and the Viterbi detector is small, the joint  $2T$  detector is not the optimal detector in this case, since there is extra memory induced due to the delayed response of the second tag. Furthermore, it was shown that the joint  $2T$  and the Viterbi joint sequence detector coincide in the synchronous 2-tags case. It was also found that the offered BER of the detectors does not present a monotonic behaviour but rather oscillates for different delay values. Asynchronous detection has been overlooked in classic digital communications; in the era of batteryless, ultra-low cost tags, more work is clearly needed.

# Chapter 4

## Multistatic Localization of Gen2 RFID Tags

This chapter contributes to RFID direction-of-arrival (DoA) estimation and multistatic localization in the following aspects:

- A novel DoA estimation technique (ElIDoA) is offered, that utilizes RFID tag signal phase measurements obtained from two receiver-transmitter pairs;
- It is shown, that the proposed DoA estimation technique, ElIDoA, demonstrates similar performance to the MUSIC algorithm;
- A novel multistatic localization method is proposed that utilizes RFID tag signal phase measurements from three bistatic RFID readers. It is shown that the measurements form ellipses in the 2D plane that facilitate the 2D localization of the RFID tag;
- As a collateral dividend it is shown that the multistatic 2D localization algorithm could facilitate the localization of a mobile robotic platform, equipped with a Gen2 RFID tag;
- A primal extension of the proposed localization technique to the 3-rd dimension is offered;

### Chapter Organization

The rest of this chapter is organized as follows. Section 4.1 offers the system model; Section 4.2 presents the DoA estimation techniques; Section 4.3 offers the multistatic phase-based 2D localization method; finally, Section 4.4 offers a primal 3D localization study.

## 4.1 System Model

In the multistatic setup of this work a single transmitter (Tx) antenna and  $M > 1$  receiver (Rx) antennas are utilized, located at the same line (unless otherwise noted). Thus, the co-linear Tx and Rx antennas and the RFID tag define a plane; the RFID tag location on that plane is denoted as  $\mathbf{x}_T \triangleq [x_{\text{tag}} \ y_{\text{tag}}]^T$ , while similarly the reader's Tx and Rx antenna locations on that plane are denoted as  $\mathbf{x}_{\text{Tx}} \triangleq [x_{\text{Tx}} \ y_{\text{Tx}}]^T$ ,  $\mathbf{x}_{\text{Rx}}^i \triangleq [x_{\text{Rx}}^i \ y_{\text{Rx}}^i]^T$ ,  $i \in \{1, 2, \dots, M\}$  for each one of the  $M$  receiving reader's antennas, respectively. The end-2-end complex channel gain for path  $i$  is denoted as follows:

$$h_i = h_{\text{CT}} h_{\text{TR},i} = |h_{\text{CT}} h_{\text{TR},i}| e^{-j\phi_i} \in \mathbb{C}, \quad (4.1)$$

where  $h_{\text{CT}}$  and  $h_{\text{TR},i}$  denotes the baseband complex channel coefficients for the TX (carrier emitter) antenna-to-tag and tag-to- $i$ -th receiver antenna, respectively; furthermore,  $h_i \in \mathbb{C}$ ,  $|h_{\text{CT}} h_{\text{TR},i}| \in \mathbb{R}_+$  and  $\phi_i \in [0, 2\pi)$ . Thus, the induced phase of the propagation channel  $h_i$  can be written as follows:

$$\phi_{\text{prop},i} \equiv \phi_i = \angle h_i = \frac{2\pi}{\lambda} (d_{\text{CT}} + d_{\text{TR},i}) + \phi_i^{\text{mult}}, \quad (4.2)$$

where  $d_{\text{CT}} \triangleq \|\mathbf{x}_{\text{Tx}} - \mathbf{x}_T\|_2$  is the Euclidean distance between the Tx antenna and the RFID tag,  $d_{\text{TR},i} \triangleq \|\mathbf{x}_{\text{Rx},i} - \mathbf{x}_T\|_2$  denotes the Euclidean distance between the RFID tag and the  $i$ -th Rx antenna,  $\lambda$  stands for the carrier wavelength and  $\phi_i^{\text{mult}}$  is the phase due to multipath, during transmission of Tx and reception of Rx antenna  $i$ . In this work each Tx and Rx antenna belong to distinct software-defined radios (SDR), synchronized with an external function generator, eliminating carrier frequency offset (CFO) and phase offset (CPO) among the different Tx and Rx antennas.

The measured phase at the reader is also affected by the tag itself, since the tag's reflection coefficient depends on the terminating load, which in turn, depends on the received power at the tag; the latter is due to various reasons, including the nonlinear rectifier at the RFID tag that harvests energy from the incoming RF signal. Thus, the tag itself induces in the phase measurement a term of  $\phi_{\text{tag}}$  that depends on reader's transmit power, reader antennas locations and tag's location (since that term depends on tag's received power). In addition, there are additional delays due to cabling (corresponding to constant phase offset  $\hat{\phi}_0$ ) as well as phase noise  $\hat{\phi}_i^n$  at

the receiver chain of Rx  $i$ . Thus, the overall phase model at Rx  $i$  follows:

$$\begin{aligned}
\phi_{\text{out},i} &= \phi_{\text{prop},i} + \hat{\phi}_0 + \phi_{\text{tag}} + \hat{\phi}_i^n \\
&= \frac{2\pi}{\lambda} (d_{\text{CT}} + d_{\text{TR},i}) + \underbrace{\phi_i^{\text{mult}} + \hat{\phi}_0 + \phi_{\text{tag}} + \hat{\phi}_i^n}_{\phi_i^n} \\
&= \frac{2\pi}{\lambda} (d_{\text{CT}} + d_{\text{TR},i}) + \phi_i^n.
\end{aligned} \tag{4.3}$$

From Eq. (4.3), it can be observed that any distance  $d_{\text{CT}} + d_{\text{TR},i}$  with

$$d_{\text{CT}} + d_{\text{TR},i} = \lambda \frac{\phi_{\text{Rx},i}}{2\pi} + k_i \lambda, \quad k_i \in \mathbb{N}, \tag{4.4}$$

outputs the same phase measurement for a given value of noise. Thus, phase measurements introduce distance ambiguity that must be explicitly addressed.

RFID readers typically report a phase value in  $[-\pi, \pi)$  or  $[0, 2\pi)$ . The reader in the conducted experiments of this work was programmed to report phase in  $[0, 2\pi)$  and thus, the measured phase from the  $i$ -th Rx follows:

$$\begin{aligned}
\phi_{\text{Rx},i} &= \phi_{\text{out},i} \bmod 2\pi \\
&\stackrel{(*)}{=} \left[ \frac{2\pi}{\lambda} (d_{\text{CT}} + d_{\text{TR},i}) \bmod 2\pi + \underbrace{\phi_i^n \bmod 2\pi}_{\tilde{\phi}_i^n} \right] \bmod 2\pi \\
&= \left[ \frac{2\pi}{\lambda} (d_{\text{CT}} + d_{\text{TR},i}) \bmod 2\pi + \tilde{\phi}_i^n \right] \bmod 2\pi,
\end{aligned} \tag{4.5}$$

where at  $(*)$ , the property  $(\alpha + \beta) \bmod \gamma = [(\alpha \bmod \gamma) + (\beta \bmod \gamma)] \bmod \gamma$  was exploited and  $\tilde{\phi}_i^n$  has support in  $[0, 2\pi)$ .

#### 4.1.1 Phase-Based Preliminaries

Measured phase as in Eq. (4.3), can also be valid if it is reported using a minus rather than a plus sign, as follows,

$$\phi_{\text{out},i} = -\frac{2\pi}{\lambda} (d_{\text{CT}} + d_{\text{TR},i}) + \phi_i^n. \tag{4.6}$$

The sign of the term  $\frac{2\pi}{\lambda} (d_{\text{CT}} + d_{\text{TR},i})$ , which depends on the channels from the transmitter to the tag and from the tag to the receiver, informs whether phase is added or

subtracted to the phase of the reader.

However, the transformation from phase measurement  $\phi$  to transmitter-to-tag-to- $i$ -th receiver distance  $d_{\text{CT}} + d_{\text{TR},i}$  and vice versa, should explicitly state which formula is used; this is important since  $\phi_- \neq \phi_+$ , for phases defined as:

$$\phi_- = -\frac{2\pi}{\lambda} (d_{\text{CT}} + d_{\text{TR},i}) \bmod 2\pi, \quad (4.7)$$

$$\phi_+ = +\frac{2\pi}{\lambda} (d_{\text{CT}} + d_{\text{TR},i}) \bmod 2\pi. \quad (4.8)$$

## 4.2 Direction-of-arrival Techniques for RFID Tag Signals

### 4.2.1 Multiple Signal Classification (MUSIC)

MUSIC is probably the most popular technique for direction of arrival estimation in a wireless communications system. In this work, MUSIC is used to estimate the DoA of the signal from a *single* RFID tag. Thus, the number of receiving antennas needs to be  $N_{\text{ant}} \geq 2$ . In order to ease notation, the system model presented below assumes RN16 packet isolation has already taken place (i.e. matched filtering, DC offset cancellation and separation of the RN16 packet from the rest of the received samples), thus:

$$\mathbf{y}(t) \equiv \begin{bmatrix} y_1(t) \\ \vdots \\ y_{N_{\text{ant}}}(t) \end{bmatrix} = \mathbf{s}(\phi)x(t) + \mathbf{n}(t) = \begin{bmatrix} 1 \\ \vdots \\ e^{-j\frac{2\pi\delta x \sin(\phi)(N_{\text{ant}}-1)}{\lambda}} \end{bmatrix} x(t) + \begin{bmatrix} n_1(t) \\ \vdots \\ n_{N_{\text{ant}}}(t) \end{bmatrix}, \quad (4.9)$$

where  $\mathbf{y} \equiv \mathbf{y}(t) \in \mathbb{C}^{N_{\text{ant}} \times 1}$ ,  $\mathbf{s}(\phi)$  denotes the  $N_{\text{ant}} \times 1$  steering vector,  $x(t) \in \mathbb{C}$  denotes the backscattered symbol received by the RFID reader at time  $t$ ,  $\delta x$  denotes the distance between neighboring antennas of the array and  $\mathbf{n}(t) \sim \mathcal{CN}(\mathbf{0}_{N_{\text{ant}}}, \underbrace{N_0 W T_s}_{\sigma^2} \mathbf{I}) \equiv$

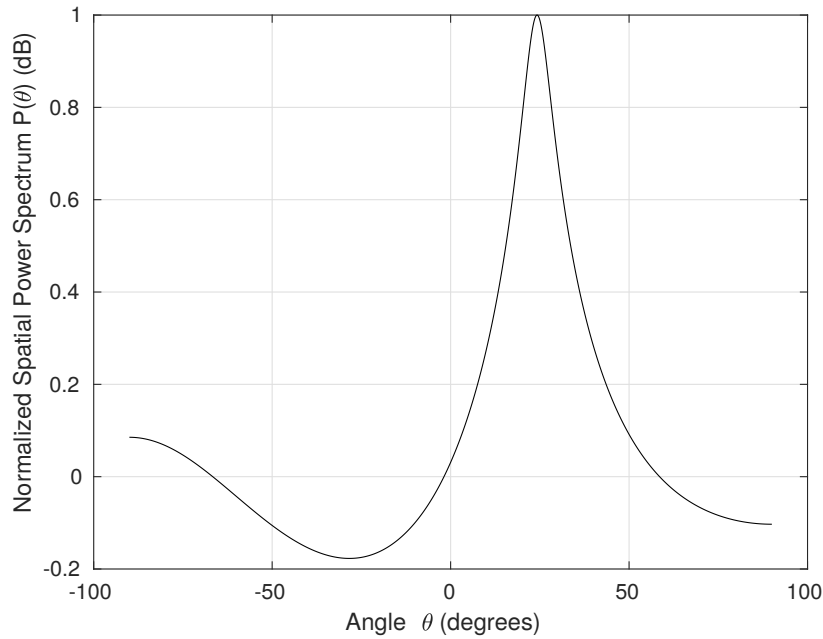


Figure 4.1: DoA estimation based on MUSIC algorithm.

$\mathcal{CN}(\mathbf{0}_{N_{\text{ant}}}, \sigma^2 \mathbf{I})$ . The correlation matrix of  $\mathbf{y}$  can be written as,

$$\begin{aligned}
 \mathbf{R} &= \mathbb{E}[\mathbf{y}\mathbf{y}^H] \\
 &= \mathbb{E}[\mathbf{s}(\phi)xx^* \mathbf{s}(\phi)^H] + \mathbb{E}[\mathbf{n}\mathbf{n}^H] \\
 &= \mathbf{s}(\phi)\|x\|_2^2 \mathbf{s}(\phi)^H + \sigma^2 \mathbf{I} \\
 &= \mathbf{R}_s + \sigma^2 \mathbf{I}.
 \end{aligned} \tag{4.10}$$

The signal covariance matrix,  $\mathbf{R}_s$ , is a  $N_{\text{ant}} \times N_{\text{ant}}$  matrix with rank 1. It therefore has  $N_{\text{ant}} - 1$  eigenvectors corresponding to the zero eigenvalue. Let  $\mathbf{q}_m$  be such an eigenvector. Therefore,

$$\begin{aligned}
 \mathbf{R}_s \mathbf{q}_m &= \mathbf{s}(\phi)\|x\|_2^2 \mathbf{s}(\phi)^H \mathbf{q}_m = 0 \\
 \Rightarrow \mathbf{q}_m^H \mathbf{s}(\phi)\|x\|_2^2 \mathbf{s}(\phi)^H \mathbf{q}_m &= 0 \\
 \Rightarrow \mathbf{s}(\phi)^H \mathbf{q}_m &= 0.
 \end{aligned} \tag{4.11}$$

Eq. (4.11) implies that all  $N_{\text{ant}} - 1$  eigenvectors  $\mathbf{q}_m$  of  $\mathbf{R}_s$  corresponding to the zero eigenvalue are orthogonal to the signal steering vector.

Call  $\mathbf{Q}_n$  the  $N_{\text{ant}} \times (N_{\text{ant}} - 1)$  matrix whose columns are these eigenvectors. MUSIC then plots the pseudo-spectrum through the use of the following function of  $\phi$ :

$$P_{\text{MUSIC}}(\phi) = \frac{1}{\|\mathbf{Q}_n^H \mathbf{s}(\phi)\|^2}. \quad (4.12)$$

Note that since the eigenvectors making up  $\mathbf{Q}_n$  are orthogonal to the signal steering vectors, the denominator becomes zero when  $\phi$  is the signal's direction. Therefore, the estimated signal direction is the largest peak in the pseudo-spectrum, also visualized in Fig. 4.1.

However, in any practical scenario, the signal covariance matrix  $\mathbf{R}_s$  would not be available. The key is that the eigenvectors in  $\mathbf{Q}_n$  can either be estimated from the eigenvectors of  $\mathbf{R}$  or equivalently  $\mathbf{Q}_n$  can be computed from the singular value decomposition (SVD) of  $\mathbf{R} = \frac{\mathbf{Y}\mathbf{Y}^H}{N_s}$ , where  $\mathbf{Y} = [\mathbf{y}(t) \ \mathbf{y}(t + T_s) \ \dots \ \mathbf{y}(t + N_s T_s)]$  and  $N_s$  the number of snapshots of data. First, the SVD of  $\mathbf{R}$  is computed as,

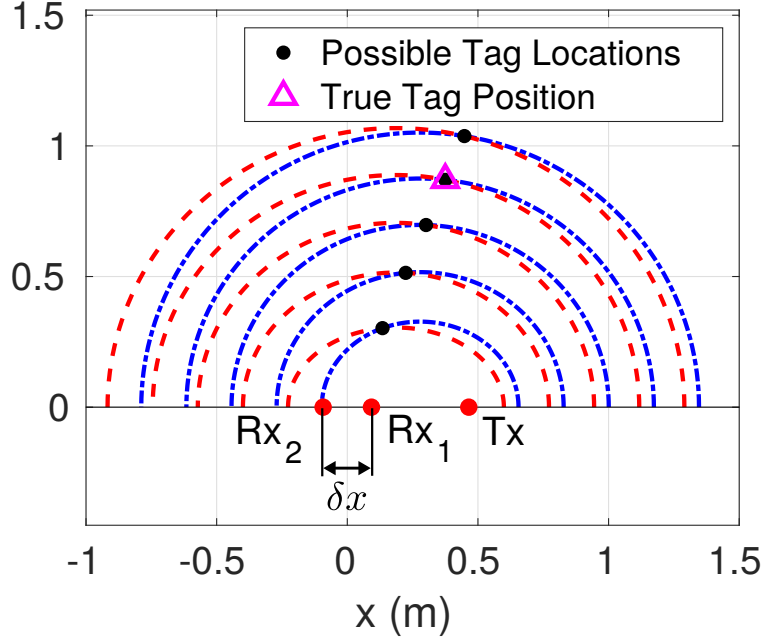
$$\mathbf{R} = \mathbf{Q} \cdot \mathbf{\Sigma} \cdot \mathbf{U}^H, \quad (4.13)$$

and second,  $\mathbf{Q}$  is partitioned to obtain  $\mathbf{Q}_n$ , corresponding to the  $(N_{\text{ant}} - 1)$  smallest eigenvalues of  $\mathbf{Q}$ , which span the noise subspace.

### 4.2.2 Multistatic Direction-of-Arrival (ElIDoA)

This work introduces a novel direction-of-arrival estimation technique, which utilizes the formation of ellipses in a bistatic RFID setup, hence the name ElIDoA. Using Eq. (4.4), the measured phase  $\phi_{\text{meas},i}$  is converted to a compound distance value  $d_{\text{CT}} + d_{\text{TR},i}$ , for a value of  $k_i \in \{0, \dots, K\}$ . The latter defines  $i$  sets of  $K$  concentric ellipses on the 2D plane. The foci of the  $i$ -th set of ellipses, are the locations of the Tx antenna and the  $i$ -th Rx antenna. In contrast to MUSIC, this technique does not require  $N_{\text{ant}} \geq 2$ , but rather,  $N_{\text{ant}} = 2$  suffices.

In order to estimate the DoA of the tag's signal, it is first necessary to compute the intersection points,  $\mathbf{p} = [p[1] \ p[2]]$ , of the two sets of ellipses, as in Fig. 4.2. A method for finding the intersection points of 2 conic sections, is given in Appendix 7.2.1. The

Figure 4.2: EllDoA method without ambiguity;  $\delta x < \lambda/2$ .

two sets of ellipses are defined as follows:

$$\frac{(x - x_1)^2}{a_1^2[k_1]} + \frac{y^2}{b_1^2[k_1]} = 1, \quad k_1 \in \{0, \dots, K\}, \quad (4.14)$$

$$\frac{(x - x_2)^2}{a_2^2[k_2]} + \frac{y^2}{b_2^2[k_2]} = 1, \quad k_2 \in \{0, \dots, K\}, \quad (4.15)$$

where  $a_i$  and  $b_i$  are the major and minor axes of the ellipses, while  $(x_1, 0)$  and  $(x_2, 0)$  are the centers of the two sets of ellipses, respectively. By convention, it is assumed that all the antennas lie upon the  $x$ -axis;  $\mathbf{x}_{\text{Tx}} \triangleq [x_{\text{Tx}} \ 0]^T$ ,  $\mathbf{x}_{\text{Rx}}^i \triangleq [x_{\text{Rx}}^i \ 0]^T$ . Hence the centers of the two ellipse sets are also located upon the  $x$ -axis. Even if the setup was to be rotated (e.g., being carried by a robotic platform), the mapping could still be translated so that all of the antennas would always lie upon the  $x$ -axis for ease of notation.

By the ellipse definition,  $d_{\text{CT}} + d_{\text{TR},i}$  is constant for any point  $(x, y)$  on the ellipse. From the latter, it can be easily shown that  $d_{\text{CT}} + d_{\text{TR},i} = 2a_i[k_i]$ , thus, for any point on the ellipse it simply follows that:

$$2a_i[k_i] = d_{\text{CT}} + d_{\text{TR},i} = \lambda \frac{\phi_{\text{Rx},i}}{2\pi} + k_i \lambda. \quad (4.16)$$

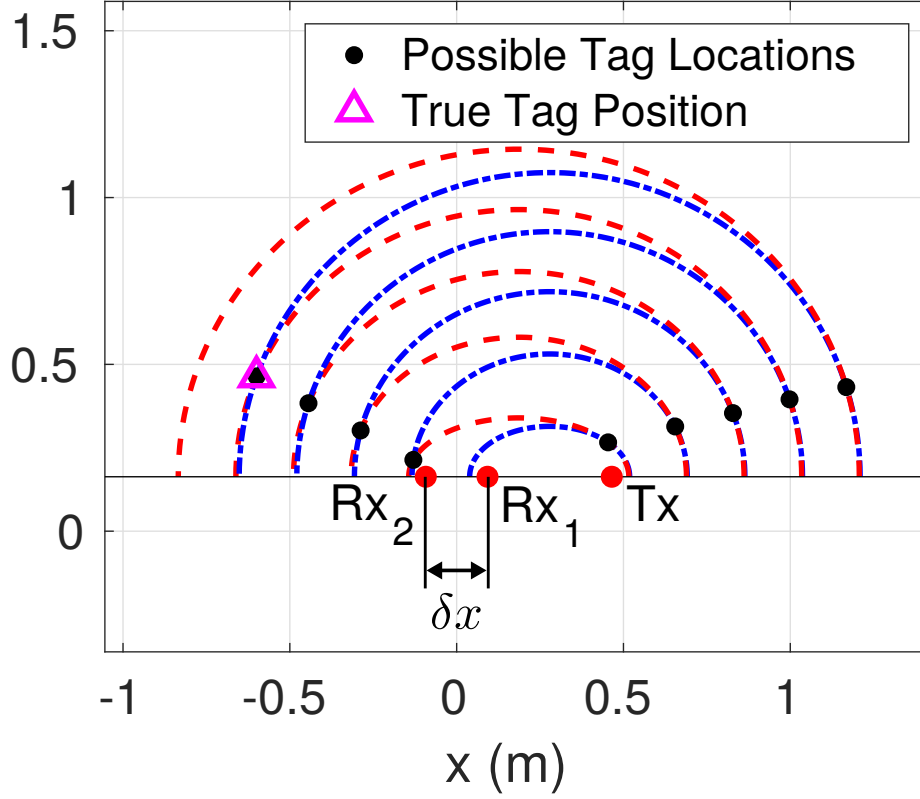


Figure 4.3: EllDoA method with ambiguity;  $\delta x > \lambda/2$ .

Since the locations of the antennas (i.e., ellipse foci) are known, the distance of the foci from the center of the ellipse, for the  $i$ -th set of ellipses, is calculated as follows:

$$c_i = \frac{|x_{\text{Tx}} - x_{\text{Rx}}^i|}{2}. \quad (4.17)$$

Notice that  $c_i$  is obviously independent of the value of  $k_i$ , since the location of the foci of the ellipse does not change as more ellipses are generated by increasing the value of  $k_i$ .

Finally, the minor axis,  $b_i[k_i]$ , of the ellipse, can be calculated by the well known ellipse formula as follows:

$$b_i[k_i] = \sqrt{a_i^2[k_i] - c_i^2}. \quad (4.18)$$

According to [45] the intersection points of the ellipses in a bistatic system, express the possible target location. However, this information is almost always ambiguous

because there are several such intersection points, so some means of identifying the correct one and rejecting the ghosts is required; such a technique will be studied in the next Section for 2D localization.

The intersection of the two sets of ellipses, stemming from the existence of two Tx-Rx pairs can offer the DoA of the signal, as shown in Fig. 4.3; in the latter figure, there is ambiguity since there are two possible directions; such ambiguity could be resolved by steering the whole antenna axis, e.g., using a robotic platform. Fortunately, such option is not necessary, as the following theorem suggests; if the spacing  $\delta x$  between the two receiving antennas satisfies  $\delta x < \lambda/2$ , the ambiguity disappears, as shown in Fig. 4.2; that is due to the smaller number of intersection points, [46], [47].

**Theorem 2.** *Assuming one Tx and two Rx antennas located at the same line, if the distance  $\delta x$  between the two receiving antennas is  $\delta x < \lambda/2$ , then a unique direction-of-arrival (DoA)  $\theta$  of the tag signal can be found, irrespectively of the Tx antenna location.*

Such unique DoA when  $\delta x < \lambda/2$  is given in close form in the following lemma:

**Lemma 4.** *Assume one Tx and two Rx antennas located at the same line,  $\phi_A \equiv \phi_{Rx,1}$ ,  $\phi_B \equiv \phi_{Rx,2}$  denote the phase at the receiving antennas, respectively and  $\alpha \triangleq \|\mathbf{x}_T - \mathbf{x}_{Rx,1}\|_2$ ,  $\beta \triangleq \|\mathbf{x}_T - \mathbf{x}_{Rx,2}\|_2$ .*

*If the distance  $\delta x$  between two receiving antennas satisfies  $\delta x < \lambda/2$ , then direction-of-arrival (DoA)  $\theta$  of the tag signal, i.e., the angle between the direction-of-arrival and the perpendicular to the line of the antennas, passing from one of the Rx antennas (from receiving antenna that offers  $\phi_A$  if  $\alpha > \beta$ , or from receiving antenna that offers  $\phi_B$  if  $\beta > \alpha$ ), is given by:*

*For  $\alpha > \beta$ ,*

$$\theta \approx \begin{cases} \sin^{-1} \left( \frac{\lambda(\phi_A - \phi_B)}{2\pi \delta x} \right), & \text{if } \phi_A > \phi_B, \\ \sin^{-1} \left( \frac{\lambda(\phi_A - \phi_B + 2\pi)}{2\pi \delta x} \right), & \text{if } \phi_A < \phi_B, \end{cases}$$

*and for  $\alpha < \beta$ ,*

$$\theta \approx \begin{cases} \sin^{-1} \left( -\frac{\lambda(\phi_A - \phi_B - 2\pi)}{2\pi \delta x} \right), & \text{if } \phi_A > \phi_B, \\ \sin^{-1} \left( -\frac{\lambda(\phi_A - \phi_B)}{2\pi \delta x} \right), & \text{if } \phi_A < \phi_B. \end{cases}$$

Both Theorem 2 and Lemma 4 assume far-field propagation, i.e., tag is located

at least  $10\lambda$  away from the antennas. Their proof is based on non-trivial geometry arguments and modulo operator properties and is omitted from this thesis work.

All in all, the following 2 conditions must be satisfied, to accurately estimate the DoA of the tag's signal:

- i) the 2 receiver antennas should be placed  $\delta x \leq \frac{\lambda}{2}$  apart,
- ii) intersection points found behind the receiver antennas are disregarded.

Choosing any of the intersection points,  $\mathbf{p}$ , that satisfy the second one of the above conditions, a DoA estimate of the tag's signal is obtained by:

$$\hat{\theta}_0 = 90^\circ - \tan^{-1} \left( \frac{p[2]}{p[1] - x_s} \right) \cdot \frac{180^\circ}{\pi}, \quad (4.19)$$

where  $x_s = (x_{\text{Rx}}^1 + x_{\text{Rx}}^2)/2$  is the  $x$ -axis coordinate of the midpoint of the 2 Rx antennas (in case they are shifted from the origin), the arctangent function  $\tan^{-1}(\cdot)$  returns values in the closed interval  $[-\pi, \pi]$  and eventually  $\hat{\theta}_0$  takes values in  $[-90^\circ, 90^\circ]$  interval. The intersection points are co-linear in this setup and thus a more robust DoA estimate can be obtained by averaging over  $K$  intersection points as follows,

$$\hat{\theta}_0 = 90^\circ - \frac{1}{K} \sum_{k=0}^{K-1} \tan^{-1} \left( \frac{p_k[2]}{p_k[1] - x_s} \right) \cdot \frac{180^\circ}{\pi}. \quad (4.20)$$

### 4.3 Multistatic 2D Localization

As already mentioned earlier, 2 ellipses (i.e., 2 receiver-transmitter pairs) do not suffice for identifying the true target location. Even though RSSI measurements could help narrow down the possible locations to perhaps a couple of points, it is not a robust distance metric and is thus neither studied nor utilized at all in this 2D/3D localization work.

Utilizing a 3-rd receiver antenna can solve the problem of ghosting. In a multistatic setup with 3 receiver antennas and 1 transmitting antenna (or vice-versa), there is *only* a single point on the 2D plane at which all 3 ellipses would simultaneously intersect. The latter can be visualized through Fig. 4.4. Thus, 2D localization with 3 transmit-receive pairs is as easy as just finding the *only* common intersection point of all 3 ellipse sets. That point must simultaneously satisfy all 3 of the following

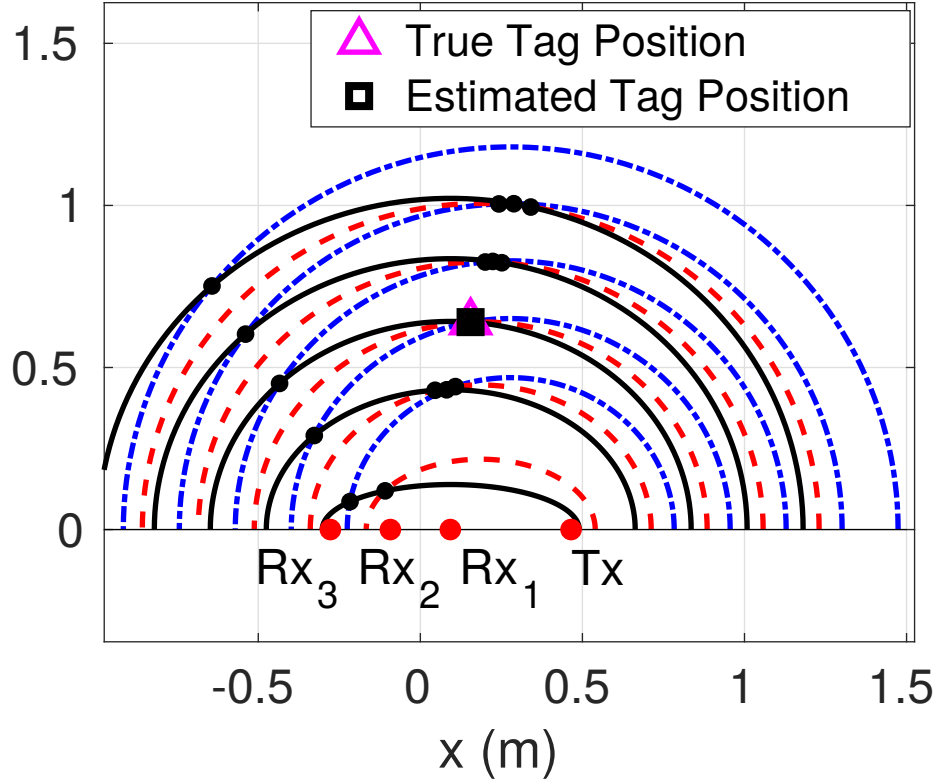


Figure 4.4: Multistatic 2D localization of an RFID tag.

equations:

$$\frac{(x - x_1)^2}{a_1^2[k_1]} + \frac{y^2}{b_1^2[k_1]} = 1, \quad (4.21)$$

$$\frac{(x - x_2)^2}{a_2^2[k_2]} + \frac{y^2}{b_2^2[k_2]} = 1, \quad (4.22)$$

$$\frac{(x - x_3)^2}{a_3^2[k_3]} + \frac{y^2}{b_3^2[k_3]} = 1, \quad (4.23)$$

where  $k_i \in \{0, \dots, K\}$ .

## 4.4 Multistatic 3D Localization

The 2D localization algorithm offered in this work, can be easily extended to the 3-rd dimension by utilizing a 4-th receiver antenna, thus, creating a 4-th bistatic (receiver-transmitter) pair. The 4-th receiver antenna will help estimate the tag's location in 3D space, however, it *must not* be placed co-linearly with the other three

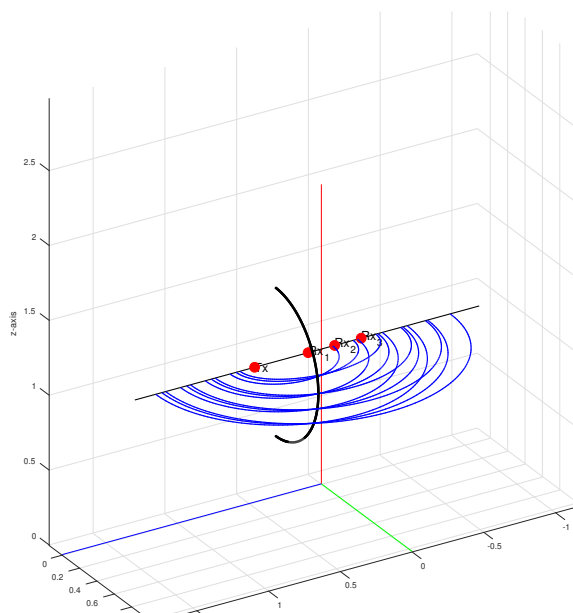


Figure 4.5: Possible tag locations in 3D, lying upon a half-circle.

receiving antennas since that would not offer any more information useful to localizing the tag in 3 dimensions.

Let us assume a tag that is not necessarily placed at the same height as the antennas of the multistatic RFID reader. The 2D localization method, utilizing the 3 co-linear Rx antennas, can estimate the 2D location of the tag assuming it is at the same height as the reader's antennas, according to the methodology in Sec. 4.3. The result of the 2D localization method is a possible tag location upon the same plane (height) as the reader's antennas, but not certainly the correct one, since we have assumed the tag's height is unknown. To find all possible tag locations, the ellipses would 'pitch up and down' like a door hinge, revealing all possible tag locations, that lie upon a half-circle. Thus, the closest estimate the 2D algorithm could offer, are the possible tag locations narrowed down to points on a half-circle, as in Fig. 4.5.

To further narrow down the possible tag locations to a single one upon the circle, a 4-th Rx antenna is necessary. The 4-th Rx antenna was placed above Rx antenna 1, but at a different height, forming a 4-th set of  $K$  ellipses (as a bistatic pair with the Tx antenna). It can be shown, that there exists only a single intersection point of that new set of ellipses with the half-circle and that is the location of the tag, as portrayed in Fig. 4.6. The proof of the latter falls out of the context of this primal 3D localization study and is thus omitted.

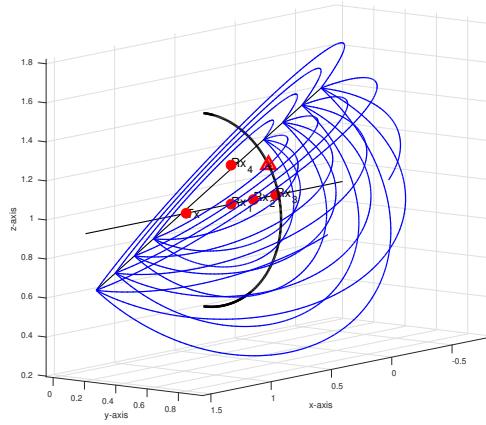


Figure 4.6: Estimated tag location in 3D, utilizing a 4-th Rx antenna.

# Chapter 5

## Simulation & Experimental Evaluation of Multistatic Localization

In this chapter, performance evaluation of the proposed DoA estimation and 2D/3D localization algorithms is conducted, via MATLAB simulations as well as with experimental data. Commodity Gen2 RFID tags were used and implementation of the proposed scheme in MATLAB and software-defined radio.

### 5.1 Experimental Evaluation of MUSIC and EIIDoA

In all experiments, a single Gen2 UHF RFID tag (ZEBRA 4" × 2" Z-PERFORM 1500T) was attached to an empty box. The experimental setup, shown in Fig. 5.1, included two USRP N200 SDR devices equipped with an SBX-40 daughterboard each, implementing a multistatic RFID reader according to the software stack in [2]; 2 circularly-polarized MTI MT-242032 antennas (both for Rx) with a gain of 7 dBic each and a single FlexiRay SF-2110 5 dBi antenna (for Tx). All of the antennas as well as the RFID tag, were placed at the same height at all times. In an attempt to quantify how multipath affected the DoA estimation methods, three different antenna (and tag) heights were tested in the experiments, 0.9 m, 1.2 m and 1.5 m. There was no point in testing bigger heights since then the multipath component from the ceiling would also start to affect the phase measurements. A Siglent SDG2042X function generator was used to provide the two USRPs with common 10 MHz reference clock and 1PPS input, using equal length cables. UHD Timed commands (see App. 7.3.1) were used in the GNURadio generated python code to synchronize the two USRPs according to the guidelines of Ettus Research. It was observed, that the two USRPs had no carrier frequency offset (CFO), but would still have 4 constant and randomly

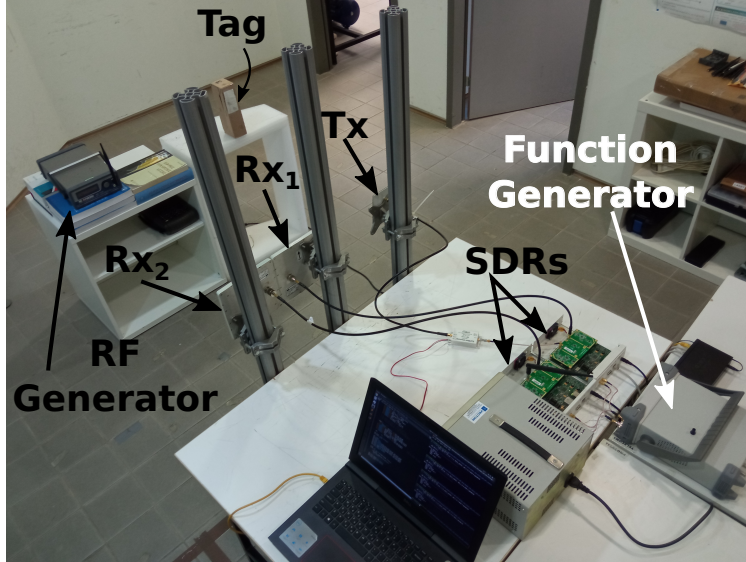


Figure 5.1: Experimental setup for DoA estimation.

repeating phase offsets. Thus, an RF signal generator was used to facilitate the residual phase offset compensation between the Rx-side local oscillators (LO) of the two SBX daughterboards. The RF signal generator was placed around 1 m away on the median of the receiver antennas at DoA = 0°, thus equidistant from both receiver antennas and was configured to emit a tone at 868 MHz at which the whole system operated. The RF signal generator would only be emitting the tone necessary for synchronization, before the RFID reader commenced the interrogation process. Reader transmission (Tx) power was configured at 25 dBm. An angle finder tool was utilized to measure the true DoA of the backscattered signal, necessary for comparison to the estimated DoA. A 24 dB Mini-Circuits ZRL-1200+ amplifier was also exploited, along with a network switch to connect the two USRP devices with the laptop computer. The total number of experiments conducted for each antenna height was  $N_{\text{exp}} = 20$ . Various angles were tested during the experiments, while the RFID tag was randomly placed from 1 m, up to 1.7 m away from the antenna array. The Mean Absolute Error was measured as follows:

$$\text{MAE} = \frac{\sum_{i=1}^{N_{\text{exp}}} |\theta_0^i - \hat{\theta}_0^i|}{N_{\text{exp}}}, \quad (5.1)$$

where  $\theta_0^i$  and  $\hat{\theta}_0^i$  are the true and estimated DoA at the  $i$ -th experiment, respectively.

As it can be clearly observed from Fig. 5.2, both direction-of-arrival estimation

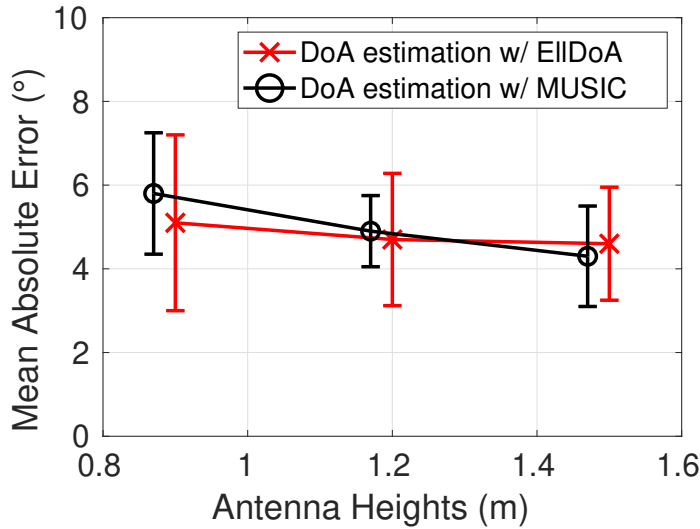


Figure 5.2: DoA mean absolute error  $\pm 1$  standard deviation.

techniques, EIIDoA and MUSIC, demonstrated almost the exact same performance throughout all of the experiments. What is more, it was stated clear that the error was reduced the higher the system was raised, due to the smaller (multi-path) impact of the ground reflection.

## 5.2 Simulation Results of 2D Localization

The ultimate purpose of this work was to implement the multistatic 2D localization method in real-time and track the trajectory of a mobile robotic platform, carrying an RFID tag and moving arbitrarily in front of the reader's antennas. Unfortunately, however, with the current equipment available at the lab, it was impossible to put this idea into practice. Nonetheless, simulations were conducted and the 2D localization results of a mobile robotic platform are presented below. The setup used in this simulation is the same as in Sec. 5.1 with a 3-rd receiver antenna, while the robot moves in a straight line in front of the antennas; from point  $(-1, 1)$  to point  $(1, 1)$ . The robot, however, could be performing any trajectory in front of the antennas and as a matter of fact, another simulated 2D localization scenario is presented in Fig. 5.3b.

In the above simulations, mean absolute localization error (MAE)  $\mathbb{E}[|e|]$  and root mean squared localization error (RMSE)  $\sqrt{\mathbb{E}[|e|^2]}$  error metrics were utilized, with  $e \triangleq \|\hat{\mathbf{x}}_T - \mathbf{x}_T\|_2$ . Phase noise  $\phi_i^n$  was treated as a random variable in the conducted

simulations and thus  $\phi_i^n \sim \mathcal{N}(0, 1^\circ)$ ,  $\phi_i^n \sim \mathcal{N}(0, 25^\circ)$  and  $\phi_i^n \sim \mathcal{N}(0, 100^\circ)$  were tested for the i.i.d. case, while  $\phi_1^n \equiv \phi_2^n \equiv \phi_3^n \equiv \phi^n \sim \mathcal{N}(0, 4\pi^2)$  was tested for the fully correlated case. The results for both phase noise definition cases are offered below. The simulation results of the two robot movement scenarios discussed above, are summarized in Table 5.1, where 100 experiments were conducted for each movement scenario and phase noise case. It should be noted, that the ellipses included in Figs. 5.3, 5.4, 5.5, 5.6, only correspond to the rightmost tag location in both cases and are just plotted as visual aid.

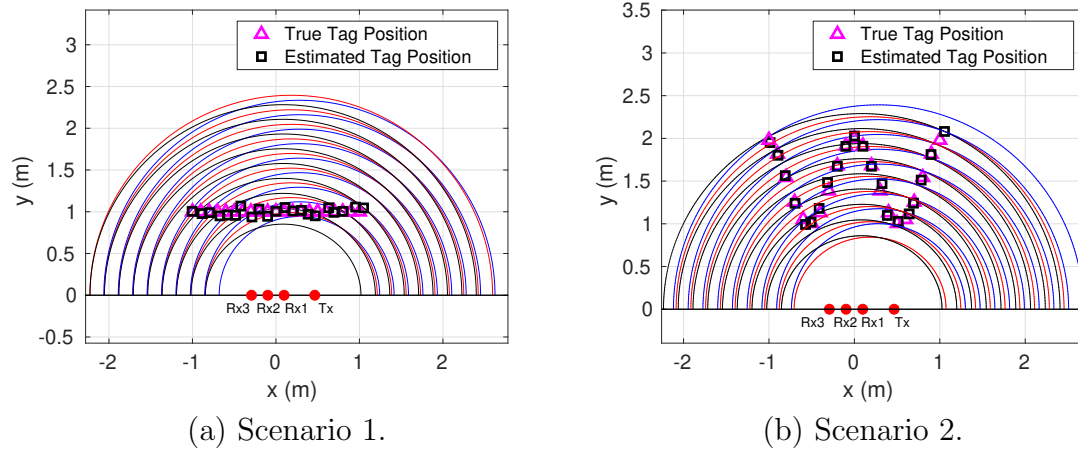


Figure 5.3: Multistatic 2D localization of a moving robotic platform, where  $\phi^n \sim \mathcal{N}(0, 4\pi^2)$  is considered fully correlated.

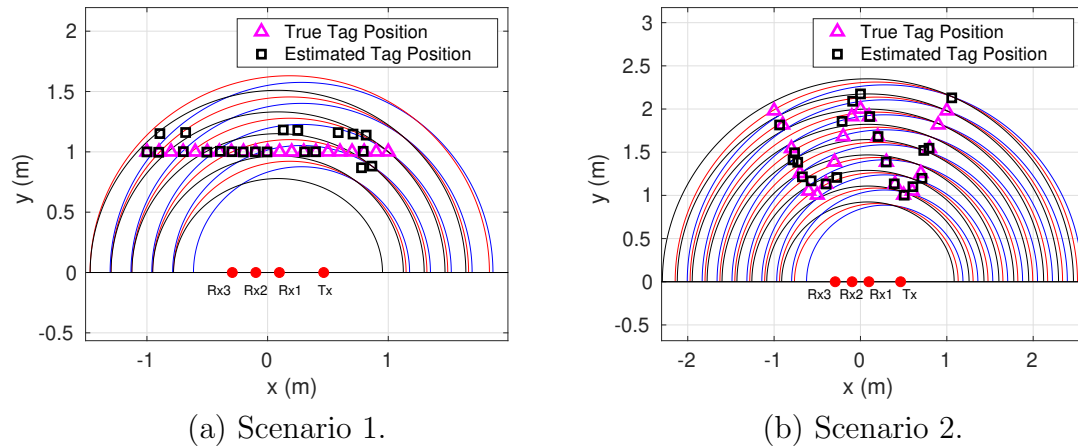


Figure 5.4: Multistatic 2D localization of a moving robotic platform, where  $\phi_i^n \sim \mathcal{N}(0, 1^\circ)$  is considered i.i.d.

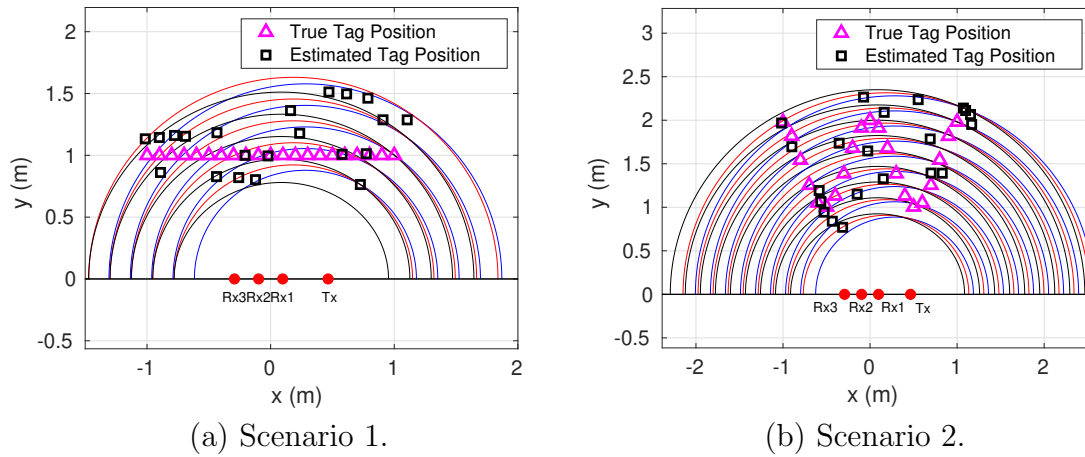


Figure 5.5: Multistatic 2D localization of a moving robotic platform, where  $\phi_i^n \sim \mathcal{N}(0, 25^\circ)$  is considered i.i.d.

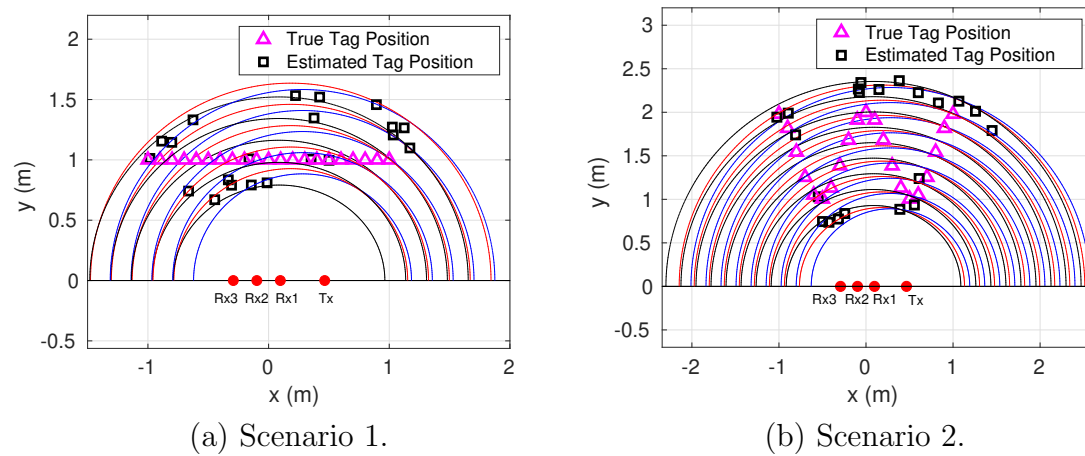


Figure 5.6: Multistatic 2D localization of a moving robotic platform, where  $\phi_i^n \sim \mathcal{N}(0, 100^\circ)$  is considered i.i.d.

	Movement Scenario	$\mathbb{E}[ \mathbf{e} ]$ (cm)	$\sqrt{\mathbb{E}[ \mathbf{e} ^2]}$ (cm)
$\phi^n \sim \mathcal{N}(0, 4\pi^2)$	Scenario 1	4.85	5.65
	Scenario 2	5.33	6.07
$\phi_i^n \sim \mathcal{N}(0, 1^\circ)$	Scenario 1	7.93	12.48
	Scenario 2	14.81	20.06
$\phi_i^n \sim \mathcal{N}(0, 25^\circ)$	Scenario 1	24.28	29.77
	Scenario 2	42.59	51.68
$\phi_i^n \sim \mathcal{N}(0, 100^\circ)$	Scenario 1	33.10	42.07
	Scenario 2	58.07	67.69

Table 5.1: Simulation results of multistatic 2D localization, considering different cases of phase noise and movement scenarios.

According to the results presented in Table 5.1, it can be deduced that in the i.i.d. phase noise case, the algorithm’s performance drastically drops with the increase in phase noise variance. Furthermore, it is observed that different robot trajectories, affect the performance of the proposed multistatic 2D localization technique, especially in the i.i.d. phase noise case. That is expected since the further away a tag moves from the receiver’s antennas, the noisier the phase measurements are expected to get (rich multipath effect), resulting in poorer performance of the localization algorithm. Last but not least, in the case of fully correlated phase noise, it can be observed that the algorithm demonstrated surprisingly low localization error around 5 cm.

### 5.3 Experimental Evaluation of 2D Localization Algorithm for RFID Tags

The measurement setup used in the multistatic 2D localization experiments is the same as the one utilized in Sec. 5.1. However, with the equipment at hand it wasn’t possible to utilize a third receiver antenna. To overcome this challenge, we decided to emulate the third receiver antenna. More specifically, after enough interrogation rounds were completed (e.g., 500 rounds), the second antenna was moved further away at a predetermined position,  $(x_{\text{Rx}}^3, y_{\text{Rx}}^3)$ , for a few more hundreds of interrogation rounds, without stopping and restarting the RFID reader. Thus, by averaging over selected time regions (i.e., when the antennas were not moving), phase measurements

Table 5.2: Experimental MAE/RMSE localization results.

Setup Height	Localization Method	Tx Power	$\mathbb{E}[ e ]$ (cm)	$\sqrt{\mathbb{E}[ e ^2]}$ (cm)
0.9 m	Multistatic	20 dBm	<b>12.85</b>	<b>13.29</b>
		25 dBm	<b>12.39</b>	<b>13.21</b>
	RDPF	20 dBm	15.24	15.74
		25 dBm	15.77	16.14
	ReLock	20 dBm	23.26	24.23
		25 dBm	17.19	17.57
1.2 m	Multistatic	20 dBm	<b>10.27</b>	<b>10.64</b>
		25 dBm	<b>10.91</b>	<b>11.73</b>
	RDPF	20 dBm	14.98	15.21
		25 dBm	15.58	16.32
	ReLock	20 dBm	19.54	20.67
		25 dBm	17.12	17.39
1.5 m	Multistatic	20 dBm	<b>9.18</b>	<b>9.98</b>
		25 dBm	<b>9.55</b>	<b>10.06</b>
	RDPF	20 dBm	15.83	16.25
		25 dBm	15.68	15.89
	ReLock	20 dBm	17.89	18.96
		25 dBm	17.38	17.68

from 3 different receiver antenna positions were eventually obtained.

The localization experiment was repeated for different setup (antennas and tag) heights; 0.9 m, 1.2 m and 1.5 m were tested. The total number of experiments conducted for each transmit power level was  $N_{\text{exp}} = 10$  (i.e., 20 experiments per antenna height value; 10 experiments per Tx power level). Transmit power levels tested were in the range of 20 and 25 dBm. During the multistatic experiments, the RFID tag was randomly placed from 0.6 m, up to 1.7 m away in front of the antenna array. A laser distance meter was utilized to measure the true location of the tag,  $(x_T, y_T)$ , as accurately as possible, necessary for calculating the algorithm's localization error. Execution times were all less than 1 sec, due to the relatively low number,  $K = 15$ , of ellipses calculated for each bistatic pair; with  $K = 15$  the three

sets of ellipses cover a distance of around 2.5 m in front of the reader's antennas, more than enough for 2D localization of an RFID tag placed up to 1.7 m away.

The multistatic phase-based 2D localization method proposed in this work was compared to the distance-based particle filtering (RDPF) method developed by our group, [17] and to ReLock [34]. For the RDPF method, the search area in front of the antenna, used for the initialization of the particles was set to  $2\text{ m} \times 2\text{ m}$ , while the number of particles was set to  $10^5$ . In both RDPF and ReLock methods, the phase measurements were gathered by the monostatic RFID reader equipped on the robotic platform of our laboratory (see Fig. 1.3). The localization results of all techniques evaluated, are offered in Table 5.2.

From Table 5.2, it can be clearly observed, that the proposed multistatic 2D localization method offered in this work, outperformed the other two methods in all cases. It was further observed, that for increasing height, the error of the proposed method was reduced (down to about 9 cm) due to the smaller (multi-path) impact of the ground reflection; Relock was found sensitive to the number of measurements (which was higher for higher Tx power), while RDPF offered a robust estimate, even though with higher error compared to this work.

## 5.4 Simulation Results of 3D Localization

The proposed 3D localization technique was only evaluated via simulations on MATLAB, due to the lack of experimental equipment necessary for its physical implementation.  $N_i = 100$  iterations were conducted, while the tag was placed at a fixed location throughout the experiments. The chosen metrics of performance were MAE and RMSE, while the same assumptions were made, regarding the phase noise, as in Section 5.2. From Table 5.3, it can be observed that the proposed 3D localization method behaves similarly to the 2D localization method, demonstrating similar accuracy (in simulation) at each phase noise case. What is more, the localization accuracy of the method seems to be very promising, clearly highlighting the necessity for experimental evaluation in the future. However, execution times were all in the range of around 1 min for a single position estimate, possibly rendering the algorithm impractical for real-time applications. The latter clearly states, that the programming of the 3D localization algorithm needs to be revised or even re-implemented in another programming language that is faster than MATLAB.

	$\mathbb{E}[ e ]$ (cm)	$\sqrt{\mathbb{E}[ e ^2]}$ (cm)
$\phi^n \sim \mathcal{N}(0, 4\pi^2)$	6.79	9.06
$\phi_i^n \sim \mathcal{N}(0, 1^\circ)$	6.93	11.93
$\phi_i^n \sim \mathcal{N}(0, 25^\circ)$	17.87	24.78
$\phi_i^n \sim \mathcal{N}(0, 100^\circ)$	30.72	35.26

Table 5.3: Simulation results of multistatic 3D localization, considering different cases of phase noise.

## 5.5 Discussion

The proposed DoA estimation technique of this work, demonstrated almost identical performance with the MUSIC algorithm. The experimental DoA estimation MAE for both techniques, was found to be in the order of  $4^\circ$ . It was further observed, that the multistatic 2D localization technique proposed in this work, offered robust performance in the presence of rich multipath that is present inside our laboratory. Centimeter-level localization error was demonstrated in the order of 9 cm, even though the system did not exploit excessive bandwidth or any reference tags. It was further confirmed via simulation, that the multistatic localization algorithm could perhaps be applied to track in real-time, the 2D motion of a robotic platform equipped with a Gen2 RFID tag. Last but not least, proof of concept was given that the 2D localization method can be extended to the 3-rd dimension by utilizing a 4-th receiving antenna. The latter, even though it could not be experimentally implemented and evaluated, it was put to test via simulation and promising centimeter-level localization accuracy was achieved, albeit with increased execution time.

# Chapter 6

## Conclusion

In this thesis, a concrete system model for the simultaneous asynchronous reception of 2 Gen2 RFID tags was developed, as well as a novel DoA estimation and 2D/3D localization techniques for Gen2 RFID tags, based upon phase measurements from a multistatic RFID reader.

### 6.1 Summary of Thesis Contributions

First and foremost, what this thesis has to offer, is an experimentally validated 2 asynchronous RFID tags collision resolution algorithm. Even though the proposed Viterbi detector supersedes by a small margin the joint  $2T$  detector, the latter is not the optimal detector in this problem because of the extra memory induced due to the delayed response of the second tag. It was also shown for the first time, that the Viterbi joint detector and the joint  $2T$  detectors coincide in the case of synchronous 2 tags transmission. It was also observed, that the offered BER of the detectors is not constantly monotonically decreasing as delay values get larger, but rather oscillates for different delay values.

Comparing the DoA estimation technique of this work to the well-known and widely used MUSIC algorithm, it was found, that the angle estimation results were just as good as when the MUSIC algorithm was applied. More specifically, the mean absolute error of both DoA estimation methods was found to be approximately  $4^\circ$ , regardless of the operating height of the setup. The multistatic 2D localization method offered in this work, presented centimeter-level localization error of an RFID tag, despite the rich multipath environment inside our laboratory. It should also be noted, that no reference tags or excessive bandwidth were utilized to achieve those results. It was also observed via simulation, that the proposed algorithm could perform 2D tracking of a mobile robotic platform equipped with a Gen2 RFID tag. The simulation results demonstrated, once again, centimeter-level localization error, which leads us to believe, that experimental evaluation of the latter would be fairly trivial with

---

the right equipment at hand. Last, the proposed 3D localization technique offered centimeter-level localization error in MATLAB simulations.

## **6.2 Direction for Future Work**

As far as asynchronous detection is concerned, future research will focus on channel estimation and packet synchronization when more than 2 tags collide, as well as the integration of the Miller line coding scheme. Regarding the multistatic 2D localization technique for RFID tags, future work would definitely try to experimentally implement real-time 2D localization of a moving robotic platform, while also analytically study and explore the 3D localization problem. Last but not least, code optimization for real-time operation of the 3D localization algorithm would make the system much more robust and efficient for practical applications.

# Chapter 7

## Appendix

### 7.1 Appendix of Chapter 2

#### 7.1.1 Proof of Theorem 1

Sampling Eq. (2.8) by  $T_s$ , the following is obtained:

$$\tilde{y}[k] \triangleq \tilde{y}(kT_s) = h_a \mu_a x_a[k] + h_b \mu_b x_b[k] + n[k], \quad (7.1)$$

where  $x_a[k] \triangleq x_a(kT_s)$ ,  $x_b[k] \triangleq x_b(kT_s) \in \{0, 1\}$  and  $n[k] \triangleq n(kT_s)$  Gaussian process with

$$\mathbb{E}[|n(kT_s)|^2] = \int_{-W}^W S_{nn}(F) dF = \frac{N_0}{2} 2W = N_0 W. \quad (7.2)$$

Thus,  $n[k] \sim \mathcal{CN}(0, \underbrace{N_0 W}_{2\sigma_n^2}) \equiv \mathcal{CN}(0, 2\sigma_n^2)$ .

The discrete baseband equivalent signal over a half-bit duration  $T/2$ , using matched filtering with rectangular pulse, for  $j = 0$  for the first half-bit and  $j = 1$  for the second half-bit, is obtained as follows:

$$\begin{aligned} y_j &= T_s \sum_{k \in \mathcal{K}_j} \tilde{y}[k] \frac{1}{\sqrt{\frac{LT_s}{2}}} = \sqrt{\frac{2T_s}{L}} \sum_{k \in \mathcal{K}_j} \tilde{y}[k] \\ &= \sqrt{\frac{2T_s}{L}} \left( \sum_{k \in \mathcal{K}_j} h_a \mu_a x_a[k] + h_b \mu_b x_b[k] \right) + n_j, \end{aligned} \quad (7.3)$$

where  $1/\sqrt{LT_s/2}$  is the appropriate normalisation factor for unit energy, corresponding to orthonormal basis functions for expansion of the received signal with duration  $T$ ,  $j \in \{0, 1\}$  and  $\mathcal{K}_0 = \{0, 1, \dots, L/2 - 1\}$ ,  $\mathcal{K}_1 = \{L/2, L/2 + 1, \dots, L - 1\}$ .

Each FM0 symbol observed with a  $T/2$  shift can be written as a  $2 \times 1$  complex vector  $\mathbf{y}_i = [y_0^i \ y_1^i]^T$ , where  $i$  denotes the  $i$ -th received  $T$ -duration symbol. With tag

$a$  perfectly synced to the detection window, one can only observe waveforms  $S_0(t)$  or  $S_1(t)$  for tag  $a$ ; however, the same does not hold for tag  $b$ . Depending on the delay of tag  $b$  RN16 response, a perfect  $S_0(t)$  or  $S_1(t)$  waveform might never be observed in the detection window, but rather a shifted combination of the two.

First,  $\tau < L/2$  is assumed, as in the example of Fig. 2.2, where tag  $a$  is emitting  $S_0(t)$  waveform, which corresponds to  $\mathbf{x}_{a,i} = \mathbf{e}_0$ ; tag  $b$  backscatters  $S_1(t)$ , delayed by  $\tau$  samples, corresponding to  $\mathbf{x}_{b,i} = \mathbf{e}_1$ . Immediately before that, tag  $b$  backscatters  $S_1(t)$ , which corresponds to  $\mathbf{x}_{b,i-1} = \mathbf{e}_1$ . Thus, according to Eq. (7.3) and the definition of  $\mathbf{y}_i$ , the following vector form is obtained for the specific signals of Fig. 2.2:

$$\begin{aligned}
\mathbf{y}_i &= \begin{bmatrix} \sqrt{\frac{2T_s}{L}} h_a \mu_a \frac{L}{2} \cdot 1 + \sqrt{\frac{2T_s}{L}} h_b \mu_b \tau \cdot 1 + n_0^i \\ \sqrt{\frac{2T_s}{L}} h_a \mu_a \frac{L}{2} \cdot 0 + \sqrt{\frac{2T_s}{L}} h_b \mu_b \left(\frac{L}{2} - \tau\right) \cdot 1 + n_1^i \end{bmatrix} \\
&= \begin{bmatrix} \sqrt{\frac{2T_s}{L}} h_a \mu_a \frac{L}{2} \cdot 1 + \sqrt{\frac{2T_s}{L}} h_b \mu_b \frac{L}{2} \left(\frac{2\tau}{L}\right) \cdot 1 + n_0^i \\ \sqrt{\frac{2T_s}{L}} h_a \mu_a \frac{L}{2} \cdot 0 + \sqrt{\frac{2T_s}{L}} h_b \mu_b \frac{L}{2} \left(1 - \frac{2\tau}{L}\right) \cdot 1 + n_1^i \end{bmatrix} \\
&= h_a \mu_a \sqrt{\frac{T}{2}} \begin{bmatrix} 1 \\ 0 \end{bmatrix} + \underbrace{\begin{bmatrix} 0 & \frac{2\tau}{L} \\ 0 & 1 - \frac{2\tau}{L} \end{bmatrix}}_{\mathbf{B}^{(i-1,i)}} h_b \mu_b \sqrt{\frac{T}{2}} \begin{bmatrix} 0 \\ 1 \end{bmatrix} + \begin{bmatrix} n_0^i \\ n_1^i \end{bmatrix}, \tag{7.4}
\end{aligned}$$

where

$$n_j^i = \sqrt{\frac{2T_s}{L}} \sum_{k \in \mathcal{K}_j} n[k] \sim \mathcal{CN} \left( 0, \underbrace{2\sigma_n^2 \left( \sqrt{\frac{2T_s}{L}} \right)^2 \frac{L}{2}}_{N_0 W T_s} \right), \tag{7.5}$$

and hence,

$$\mathbf{n}_i = [n_0^i \ n_1^i]^T \sim \mathcal{CN}(\mathbf{0}_2, N_0 W T_s \mathbf{I}_2). \tag{7.6}$$

Repeating the process above, for every scenario in Table 2.2 for  $\tau < L/2$  and once more for  $\tau \geq L/2$ , while maintaining  $\mathbf{x}_a$  in perfect sync to the detection window, yields the closed form of  $\mathbf{B}^{(i-1,i)}$  matrices offered in Table 2.1 and eventually, Eq. (2.14).

### 7.1.2 Proof of Eq. (2.18)

The expression of  $\text{SNR}_b$  for  $\tau > 0$  is calculated as follows:

$$\text{SNR}_b \triangleq \frac{\mathbb{E} \left[ \left| \mathbf{B}_{(i-1,i)} h_b \sqrt{\frac{\mathcal{E}_{bit}^b}{\mathbb{E}[|h_b|^2]}} \mathbf{x}_{b,i} \right|^2 \right]}{\mathbb{E}[|\mathbf{n}_i|^2]} = \frac{\mathbb{E} [\mathbf{x}_{b,i}^T \mathbf{B}^T \mathbf{B} \mathbf{x}_{b,i}] \mathcal{E}_{bit}^b}{2N_0 W T_s}, \quad (7.7)$$

where

$$\begin{aligned} \mathbb{E} [\mathbf{x}_{b,i}^T \mathbf{B}^T \mathbf{B} \mathbf{x}_{b,i}] &= \mathbb{E}_{\mathbf{x}_{b,i}} \left\{ \underbrace{\mathbb{E}_{\mathbf{B}|\mathbf{x}_{b,i}} [\mathbf{x}_{b,i}^T \mathbf{B}^T \mathbf{B} \mathbf{x}_{b,i}]}_{g(\mathbf{x}_{b,i})} \right\} \\ &= \frac{1}{2} g \left( \mathbf{x}_{b,i} = \begin{bmatrix} 1 \\ 0 \end{bmatrix} \right) + \frac{1}{2} g \left( \mathbf{x}_{b,i} = \begin{bmatrix} 0 \\ 1 \end{bmatrix} \right) \\ &= \frac{1}{2} [0 \quad 1] \mathbb{E} \left\{ \mathbf{B}^T \mathbf{B} \middle| \mathbf{x}_{b,i} = \begin{bmatrix} 0 \\ 1 \end{bmatrix} \right\} \begin{bmatrix} 0 \\ 1 \end{bmatrix} \\ &\quad + \frac{1}{2} [1 \quad 0] \mathbb{E} \left\{ \mathbf{B}^T \mathbf{B} \middle| \mathbf{x}_{b,i} = \begin{bmatrix} 1 \\ 0 \end{bmatrix} \right\} \begin{bmatrix} 1 \\ 0 \end{bmatrix}. \end{aligned} \quad (7.8)$$

$\mathbb{E}[\mathbf{B}^T \mathbf{B} | \mathbf{x}_{b,i}]$  in Eq. (7.8) is calculated as follows:

$$\mathbb{E}[\mathbf{B}^T \mathbf{B} | \mathbf{x}_{b,i}] = \sum_{\mathbf{B}^T \mathbf{B}} \frac{1}{4} \mathbf{B}^T \mathbf{B}. \quad (7.9)$$

For  $\mathbf{x}_{b,i} = [1 \quad 0]^T$ , according to Table 2.1,

$$\begin{aligned} \sum_{\mathbf{B}^T \mathbf{B}} \frac{1}{4} \mathbf{B}^T \mathbf{B} &= \frac{1}{4} \left( \underbrace{\mathbf{B}_1^T \mathbf{B}_1 + \mathbf{B}_3^T \mathbf{B}_3}_{\tau < L/2} + \underbrace{\mathbf{B}_1^T \mathbf{B}_1 + \mathbf{B}_3^T \mathbf{B}_3}_{\tau \geq L/2} \right) \\ &= \frac{1}{4} \begin{bmatrix} \frac{12L^2 - 24\tau L + 24\tau^2}{L^2} & 0 \\ 0 & 0 \end{bmatrix}. \end{aligned} \quad (7.10)$$

Notice that the two  $\mathbf{B}_j^T \mathbf{B}_j$  products are for a different range of  $\tau$  values.

For  $\mathbf{x}_{b,i} = [0 \ 1]^T$  and according to Table 2.1 in the same fashion,

$$\begin{aligned} \sum_{\mathbf{B}^T \mathbf{B}} \frac{1}{4} \mathbf{B}^T \mathbf{B} &= \frac{1}{4} \left( \underbrace{\mathbf{B}_2^T \mathbf{B}_2 + \mathbf{B}_4^T \mathbf{B}_4}_{\tau < L/2} + \underbrace{\mathbf{B}_2^T \mathbf{B}_2 + \mathbf{B}_4^T \mathbf{B}_4}_{\tau \geq L/2} \right) \\ &= \frac{1}{4} \begin{bmatrix} 0 & 0 \\ 0 & \frac{8L^2 - 24\tau L + 24\tau^2}{L^2} \end{bmatrix}. \end{aligned} \quad (7.11)$$

Substituting Eqs. (7.10) and (7.11) into Eq. (7.8) we obtain:

$$\begin{aligned} \mathbb{E}[\mathbf{x}_{b,i}^T \mathbf{B}^T \mathbf{B} \mathbf{x}_{b,i}] &= \frac{1}{2} [1 \ 0] \frac{1}{4} \begin{bmatrix} \frac{12L^2 - 24\tau L + 24\tau^2}{L^2} & 0 \\ 0 & 0 \end{bmatrix} \begin{bmatrix} 1 \\ 0 \end{bmatrix} + \frac{1}{2} [0 \ 1] \frac{1}{4} \begin{bmatrix} 0 & 0 \\ 0 & \frac{8L^2 - 24\tau L + 24\tau^2}{L^2} \end{bmatrix} \begin{bmatrix} 0 \\ 1 \end{bmatrix} \\ &= \frac{\frac{5}{2}L^2 - 6L\tau + 6\tau^2}{L^2}. \end{aligned} \quad (7.12)$$

Eventually, substituting Eq. (7.12) into Eq. (7.7) we obtain:

$$\text{SNR}_b = \frac{(5L^2 - 12\tau L + 12\tau^2) \mathcal{E}_{bit}^b}{4N_0 W T_s L^2}. \quad (7.13)$$

### 7.1.3 Proof of Eq. (2.20)

The baseband complex channel coefficients  $h_{T_a R}$  and  $h_{T_b R}$  are independent random variables following the Rician distribution according to [39], with parameters  $\kappa_m = \frac{s^2}{2\sigma_g^2}$ , where  $s^2 = \frac{\rho \kappa_m}{\kappa_m + 1}$ ,  $2\sigma_g^2 = \frac{\rho}{\kappa_m + 1}$  and  $\rho \equiv \sigma_{h_{T_m R}}^2$ . According to [48, Eq. (50)], the

$k$ -th moment of the Rician (Nakagami- $n$ ) distribution is calculated as follows:

$$\begin{aligned}
\mathbb{E}[|h_{\Gamma_m\text{R}}|^k] &\triangleq (2\sigma_g^2)^{k/2} \Gamma\left(1 + \frac{k}{2}\right) {}_1F_1\left(-\frac{k}{2}; 1; -\frac{s^2}{2\sigma_g^2}\right) \\
&\stackrel{k=4}{=} 4\sigma_g^4 \Gamma(3) {}_1F_1\left(-2; 1; -\frac{s^2}{2\sigma_g^2}\right) = 8\sigma_g^4 \left(1 + \frac{s^2}{\sigma_g^2} + \frac{s^4}{8\sigma_g^4}\right) \\
&= 8\sigma_g^4 + 8\sigma_g^2 s^2 + s^4 = 2(2\sigma_g^2)^2 + 4(2\sigma_g^2)s^2 + s^4 \\
&= 2\left(\frac{\rho}{\kappa_m + 1}\right)^2 + 4\left(\frac{\rho}{\kappa_m + 1}\right)s^2 + s^4 \\
&= 2\left(\frac{\rho}{\kappa_m + 1}\right)^2 + 4\left(\frac{\rho}{\kappa_m + 1}\right)^2 + \left(\frac{\rho \kappa_m}{\kappa_m + 1}\right)^2 \\
&= \frac{\rho^2 (\kappa_m^2 + 4\kappa_m + 2)}{(\kappa_m + 1)^2} = \frac{(\sigma_{h_{\Gamma_m\text{R}}}^2)^2 (\kappa_m^2 + 4\kappa_m + 2)}{(\kappa_m + 1)^2}, \tag{7.14}
\end{aligned}$$

where  ${}_1F_1(\cdot)$  denotes the confluent hypergeometric function.

## 7.2 Appendix of Chapter 4

### 7.2.1 Intersection of 2 Conic Sections

The proof of the intersection of 2 conic sections is based on the book of Richter-Gebert Jrgen, [49]. In general 2 conic sections (ellipses, hyperbolas, parabolas) can either not intersect at all, or intersect at up to 4 points. Since this work deals with ellipses, it is known that an ellipse can be transformed from the standard ellipse equation expressed in Eqs. (4.14),(4.15), to the general form of an equation of a conic section, which is defined as:

$$Ax^2 + 2Bxy + Cy^2 + 2Dx + 2Ey + F = 0. \tag{7.15}$$

As a sidenote, if  $B^2 - 4AC < 0$ , then the conic section is definitely an ellipse. Expanding Eqs. (4.14),(4.15) to the form of Eq. (7.15) we obtain:

$$b_1^2[k_1]x^2 + a_1^2[k_1]y^2 - 2b_1^2[k_1]x_1x + (b_1^2[k_1]x_1^2 - a_1^2[k_1]b_1^2[k_1]) = 0, \tag{7.16}$$

$$b_2^2[k_2]x^2 + a_2^2[k_2]y^2 - 2b_2^2[k_2]x_2x + (b_2^2[k_2]x_2^2 - a_2^2[k_2]b_2^2[k_2]) = 0. \tag{7.17}$$

Eqs. (7.16),(7.17) can be further transformed using the matrix representation of conic sections, which according to Eq. (7.15) is defined as follows:

$$\begin{bmatrix} x & y & 1 \end{bmatrix} \underbrace{\begin{bmatrix} A & B & D \\ B & C & E \\ D & E & F \end{bmatrix}}_{\mathbf{C}} \begin{bmatrix} x \\ y \\ 1 \end{bmatrix} = 0, \quad (7.18)$$

where  $\mathbf{C} \in \mathbb{R}^{3 \times 3}$ . Hence, according to Eq. (7.18) we obtain:

$$\mathbf{C}_1 = \begin{bmatrix} b_1^2[k_1] & 0 & -b_1^2[k_1]x_1 \\ 0 & a_1^2[k_1] & 0 \\ -b_1^2[k_1]x_1 & 0 & (b_1^2[k_1]x_1^2 - a_1^2[k_1]b_1^2[k_1]) \end{bmatrix}, \quad (7.19)$$

for Eq. (7.16) and

$$\mathbf{C}_2 = \begin{bmatrix} b_2^2[k_2] & 0 & -b_2^2[k_2]x_2 \\ 0 & a_2^2[k_2] & 0 \\ -b_2^2[k_2]x_2 & 0 & (b_2^2[k_2]x_2^2 - a_2^2[k_2]b_2^2[k_2]) \end{bmatrix}, \quad (7.20)$$

for Eq. (7.17).

The following algorithm roughly describes the process that will be followed to obtain the intersection points, omitting any formulas.

---

**Algorithm 1:** Intersection of 2 conic sections

---

**Input:**  $\mathbf{C}_1, \mathbf{C}_2$

**Output:**  $\mathbf{p}$

- 1 Calculate  $\mathbf{C}_\lambda = \mu\mathbf{C}_1 + \lambda\mathbf{C}_2$  such that  $(\lambda, \mu) \neq (0, 0)$  and  $\det(\mathbf{C}_\lambda) = 0$
  - 2 Create a degenerate conic  $\mathbf{C}_d$  for some  $(\lambda, \mu)$  that are solutions to Step 1
  - 3 Split the degenerate conic  $\mathbf{C}_d$  into two lines  $\mathbf{l}$  and  $\mathbf{m}$
  - 4 Intersect both lines  $\mathbf{l}$  and  $\mathbf{m}$  with the conics  $\mathbf{C}_1$  and  $\mathbf{C}_2$
- 

To estimate the intersection numerically, the following pencil of conics, that contains both conics  $\mathbf{C}_1$  and  $\mathbf{C}_2$ , is constructed,

$$\mathbf{C}_\lambda = \mu\mathbf{C}_1 + \lambda\mathbf{C}_2. \quad (7.21)$$

We exploit the conic of the pencil that is represented by straight lines intersecting both points  $\mathbf{p}_1$  and  $\mathbf{p}_2$ . This is a degenerate conic (a set of straight lines) whose conic

matrix determinant is vanishing.

Setting  $\mu = 1$  to simplify things, lets us just looking for a value  $\lambda \neq 0$  such that  $\det(\mathbf{C}_\lambda) = 0$ . To find  $\lambda$  the characteristic polynomial of the pencil of conics is necessary, but before that the pencil of conics is transformed accordingly,

$$-(\mathbf{C}_1 + \lambda\mathbf{C}_2) \cdot (\mathbf{C}_2)^{-1} = \lambda\mathbf{I} - \mathbf{C}_1 \cdot (\mathbf{C}_2)^{-1} = \lambda\mathbf{I} - \mathbf{A}. \quad (7.22)$$

It can be easily observed that solving  $\det(\mathbf{C}_1 + \lambda\mathbf{C}_2) = 0$  is equivalent to solving  $\det(\lambda\mathbf{I} - \mathbf{A}) = 0$ . In this new formulation,  $\lambda$  represents the eigenvalue of matrix  $\mathbf{A}$  and  $\det(\lambda\mathbf{I} - \mathbf{A})$  is the characteristic polynomial of  $\mathbf{A}$ . The characteristic polynomial of  $\mathbf{A}$  (which is a  $3 \times 3$  matrix) can be written as:

$$-\lambda^3 + \lambda^2\text{Tr}(\mathbf{A}) - \frac{\lambda}{2} (\text{Tr}^2(\mathbf{A}) - \text{Tr}(\mathbf{A}^2)) + \det(\mathbf{A}) = 0, \quad (7.23)$$

which has 3 possible solutions (some of the solutions might me double or even complex) denoted as  $\lambda_1, \lambda_2, \lambda_3$ . Picking a real valued solution out of the 3 and plugging it into the pencil of Eq. (7.21), a degenerate conic of the pencil can be identified. In particular one of the 3 solutions gives,

$$\mathbf{C}_d = \mathbf{C}_1 + \lambda\mathbf{C}_2, \quad \lambda \in \{\lambda_1, \lambda_2, \lambda_3\}, \quad (7.24)$$

whose determinant is zero. Since  $\mathbf{C}_d$  is a degenerate conic its rank will either be 1 or 2. Having the matrix representation of the degenerate conic, it can now be decomposed, according to its rank. If  $\text{rank}(\mathbf{C}_d) = 1$ , then the degenerate conic  $\mathbf{C}_d$  can be decomposed to two coincident straight lines of the form:

$$\mathbf{C}_d = \mathbf{l}^T \cdot \mathbf{l}. \quad (7.25)$$

To decompose  $\mathbf{C}_d$  into  $\mathbf{l}$  we can simply pick the  $i$ -th row (and the  $j$ -th column) of  $\mathbf{C}_d$  related to any of the non-vanishing element  $C_{ij}$ .

In case  $\text{rank}(\mathbf{C}_d) = 2$ , then the degenerate conic is composed by two intersecting lines  $\mathbf{l}$  and  $\mathbf{m}$  and their intersection point  $\mathbf{p}$ ,

$$\mathbf{C}_d = \mathbf{m} \cdot \mathbf{l}^T + \mathbf{l} \cdot \mathbf{m}^T. \quad (7.26)$$

Moreover, any point on one of the two lines  $\mathbf{l}$  or  $\mathbf{m}$  belongs to the conic. If  $\mathbf{p}$  is on  $\mathbf{l}$

then  $\mathbf{l} \cdot \mathbf{p} = 0$  and

$$\mathbf{p}^T \mathbf{C} \mathbf{p} = \mathbf{p}^T \mathbf{l}^T \cdot \mathbf{m} \mathbf{p} + \mathbf{p}^T \mathbf{m}^T \cdot \mathbf{l} \mathbf{p} = 0 \cdot \mathbf{m} \mathbf{p} + \mathbf{p}^T \mathbf{m}^T \cdot 0 = 0, \quad (7.27)$$

similarly, this can be proven for any point  $\mathbf{q}$  on line  $\mathbf{m}$ . To decompose this matrix we are going to recover the intersection point  $\mathbf{p}$  and subsequently the matrix  $\mathbf{l}^T \cdot \mathbf{m}$ .

To localize  $\mathbf{p}$  we employ the dual conic  $\mathbf{U}$  associated to  $\mathbf{C}_d$ . A dual conic represents the locus of all the tangent lines to  $\mathbf{C}_d$ . In particular, it can be demonstrated that this locus is still represented by a quadratic form and its matrix form is given by  $\mathbf{U}$ , which is the adjoint matrix of  $\mathbf{C}_d$ . The dual conic is composed by a double point representing the intersection point of the original degenerate conic's straight lines  $\mathbf{l}$  and  $\mathbf{m}$ .

The intersection point is thus easily recovered given matrix  $\mathbf{U}$ , by taking the matrix column  $\mathbf{U}_j$  related to a non-vanishing element  $U_{ij}$ . In particular,

$$\mathbf{p} = \frac{1}{U_{ij}} \mathbf{U}_j. \quad (7.28)$$

The intersection point  $\mathbf{p}$  can be seen as  $\mathbf{p} = \mathbf{l} \times \mathbf{m}$ . Moreover, given  $\mathbf{p}$  we can recover the matrix  $\mathbf{S}_p \equiv \mathbf{S}_{\mathbf{l} \times \mathbf{m}}$ , where  $\mathbf{S}_p$  is the skew symmetric matrix associated to the vector  $\mathbf{p}$ . If we now consider,

$$\mathbf{V} = \mathbf{C} + \mathbf{S}_{\mathbf{l} \times \mathbf{m}}, \quad (7.29)$$

we can expand it to obtain:

$$\mathbf{V} = \mathbf{l}^T \cdot \mathbf{m} + \mathbf{m}^T \cdot \mathbf{l} + \mathbf{S}_p. \quad (7.30)$$

By expanding each single element this can be transformed into:

$$\mathbf{V} = 2\mathbf{l}^T \cdot \mathbf{m}, \quad (7.31)$$

which is a rank 1 (non-symmetric) matrix. We can then perform the rank 1 decomposition, described above, to recover  $\mathbf{l}$  and  $\mathbf{m}$  given  $\mathbf{V}$ . Given a non-vanishing value  $V_{ij}$  the two lines can be recovered as:

$$\mathbf{l} \propto V_i, \quad \mathbf{m} \propto V_j^T. \quad (7.32)$$

Having obtained now the two lines we can calculate their intersection with the two conics  $\mathbf{C}_1$  and  $\mathbf{C}_2$ , where up to four possible intersection points can be obtained  $\mathbf{p}_1$ ,  $\mathbf{p}_2$ ,  $\mathbf{p}_3$  and  $\mathbf{p}_4$ . This is done by solving the following four systems:

$$\begin{cases} \mathbf{p}_1^T \cdot \mathbf{C}_1 \cdot \mathbf{p}_1 & = 0 \\ \mathbf{l} \cdot \mathbf{p}_1 & = 0 \end{cases}, \quad (7.33)$$

$$\begin{cases} \mathbf{p}_2^T \cdot \mathbf{C}_1 \cdot \mathbf{p}_2 & = 0 \\ \mathbf{m} \cdot \mathbf{p}_2 & = 0 \end{cases}, \quad (7.34)$$

$$\begin{cases} \mathbf{p}_3^T \cdot \mathbf{C}_2 \cdot \mathbf{p}_3 & = 0 \\ \mathbf{l} \cdot \mathbf{p}_3 & = 0 \end{cases}, \quad (7.35)$$

$$\begin{cases} \mathbf{p}_4^T \cdot \mathbf{C}_2 \cdot \mathbf{p}_4 & = 0 \\ \mathbf{m} \cdot \mathbf{p}_4 & = 0 \end{cases}. \quad (7.36)$$

Some of the points might not have real elements. In that case these points are disregarded and only the ones with the real elements are kept. If all points have complex elements then the two ellipses do not have any intersection points.

## 7.2.2 Proof of EllDoA

Assume a bistatic system of the setup portrayed in Fig. 7.1. Further assume a single intersection point  $\mathbf{p}$  of the 2 ellipses. In particular, it can be shown that if  $\delta x \leq \lambda/2$ , then  $\mathbf{p}$  is produced for  $k_1 = i$  and  $k_2 = j$ , where  $i$  is not necessarily equal to  $j$ . The intersection point satisfies the following equations:

$$d_{\text{CT}} + d_{\text{TR},1} = 2a_1[k_1] = \lambda \frac{\phi_{\text{out},1}}{360^\circ} + k_1\lambda, \quad (7.37)$$

$$d_{\text{CT}} + d_{\text{TR},2} = 2a_2[k_2] = \lambda \frac{\phi_{\text{out},2}}{360^\circ} + k_2\lambda. \quad (7.38)$$

Subtracting the second equation from the first yields:

$$d_{\text{TR},1} - d_{\text{TR},2} = \lambda \left( \frac{\phi_{\text{out},1} - \phi_{\text{out},2}}{360^\circ} + k_1 - k_2 \right). \quad (7.39)$$

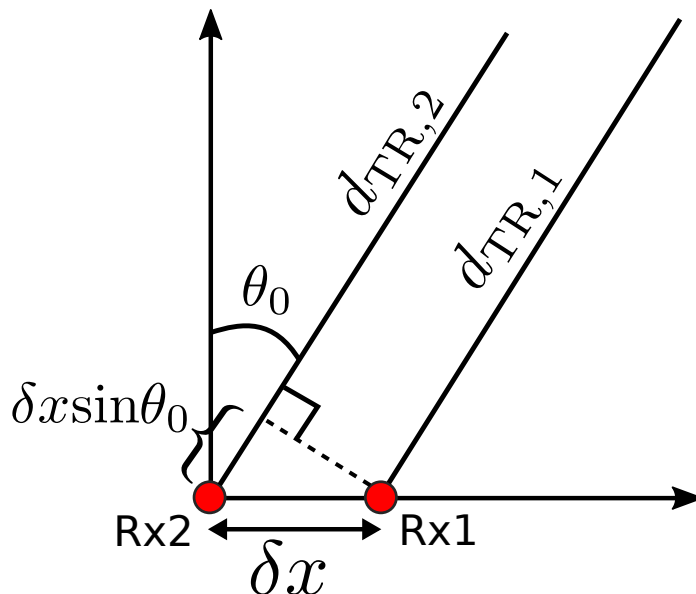


Figure 7.1: EllDoA receiver topology and angle of arrival.

Assuming far-field propagation, then from Fig. 7.1 it can be shown that,

$$d_{TR,2} = d_{TR,1} + \delta x \sin \theta_0, \quad (7.40)$$

where  $\theta_0$  is the angle of arrival of the tag's signal. Substituting Eq. (7.40) into Eq. (7.39) we obtain:

$$\theta_0 = \sin^{-1} \left( -\frac{\lambda}{\delta x} \left( \frac{\phi_{out,1} - \phi_{out,2}}{360^\circ} + k_1 - k_2 \right) \right). \quad (7.41)$$

Thus, starting from a single intersection point  $\mathbf{p}$  of the 2 ellipses, we have shown that  $\mathbf{p}$  is indeed at the direction-of-arrival of the signal. To prove that the set of intersection points are co-linear is now trivial and can be quickly proven by induction.

■

## 7.3 Appendix of Chapter 5

### 7.3.1 Synchronization of 2 USRP N200 SDRs using UHD Timed Commands

As it was already stated in Ch. 4 the USRP devices utilized in this work need to be synchronized in order to ensure a predictable and repeatable phase offset between

the receive channels of the USRPs. There are four key elements required for phase coherent operation of resync-capable USRPs:

- 1) All USRPs share a common reference clock (10MHz Ref)
- 2) All USRPs share a common sense of time (PPS)
- 3) LO and DSP tuning is synchronous
- 4) Streaming is started synchronously

LO sharing is implemented in some USRP products such as the SBX-40 daughterboards. The code that achieves 3) and 4) in software, assuming that the physical connections required in 1) and 2) are already satisfied, is offered below:

---

```
1  def usrp_init(self):
2      self.sink = uhd.usrp_sink(
3          ", ".join(("addr0=192.168.10.2,addr1=192.168.10.3", "")),
4          uhd.stream_args(
5              cpu_format="fc32",
6              channels=range(2),
7          ),
8      )
9
10     self.source = uhd.usrp_source(
11         ", ".join(("addr0=192.168.10.2,addr1=192.168.10.3", "")),
12         uhd.stream_args(
13             cpu_format="fc32",
14             channels=range(2),
15         ),
16     )
17
18     self.source.set_clock_source('external', 0)
19     self.source.set_time_source('external', 0)
20     self.source.set_clock_source('external', 1)
21     self.source.set_time_source('external', 1)
22     self.sink.set_clock_source('external', 0)
23     self.sink.set_time_source('external', 0)
24     self.sink.set_clock_source('external', 1)
25     self.sink.set_time_source('external', 1)
26     self.source.set_time_unknown_pps(uhd.time_spec(0.0))
27     self.sink.set_time_unknown_pps(uhd.time_spec(0.0))
28     self.source.set_samp_rate(self.adc_rate)
```

---

```
29     self.source.set_gain(self.rx_gain0,0)
30     self.source.set_gain(self.rx_gain1,1)
31     self.source.set_antenna("RX2")
32     self.sink.set_samp_rate(self.dac_rate)
33     self.sink.set_gain(self.tx_gain0, 0)
34     self.sink.set_gain(0, 1)
35     self.sink.set_antenna("TX/RX")
36
37     time.sleep(1)
38
39     self.source.clear_command_time()
40     self.sink.clear_command_time()
41
42     self.source.set_command_time(self.source.get_time_now() + uhd.time_spec_t(0.1));
43     self.sink.set_command_time(self.sink.get_time_now() + uhd.time_spec_t(0.1));
44
45     trequest = uhd.tune_request(868e6, args=uhd.device_addr('mode_n=integer'))
46     self.source.set_center_freq(trequest,0)
47     self.source.set_center_freq(trequest,1)
48     self.sink.set_center_freq(trequest,0)
49     self.sink.set_center_freq(trequest,1)
50
51     self.source.clear_command_time()
52     self.sink.clear_command_time()
```

---

# References

- [1] “EPC Radio-Frequency Identity Protocols, Class-1 Generation-2 UHF RFID Protocol for Communications at 860 MHz - 960 MHz, version 1.2.0 EPC Global,” 2008.
- [2] N. Kargas, F. Mavromatis, and A. Bletsas, “Fully-coherent reader with commodity SDR for Gen2 FM0 and computational RFID,” *IEEE Wireless Commun. Lett.*, vol. 4, no. 6, pp. 617–620, Dec. 2015.
- [3] D. Shen, G. Woo, D. P. Reed, A. B. Lippman, and J. Wang, “Separation of multiple passive RFID signals using software defined radio,” in *Proc. IEEE Int. Conf. on RFID*, Orlando, FL, Apr. 2009, pp. 139–146.
- [4] C. Angerer, G. Maier, M. V. Delgado, M. Rupp, and J. V. Alonso, “Single antenna physical layer collision recover receivers for RFID readers,” in *Proc. IEEE Int. Conf. on Industrial Technology (ICIT)*, Vina del Mar, Chile, Mar. 2010, pp. 1406–1411.
- [5] C. Angerer, R. Langwieser, and M. Rupp, “RFID reader receivers for physical layer collision recovery,” *IEEE Trans. Commun.*, vol. 58, no. 12, pp. 3526–3537, Dec. 2010.
- [6] J. Kaitovic, R. Langwieser, and M. Rupp, “RFID reader with multi antenna physical layer collision recovery receivers,” in *Proc. IEEE Int. Conf. on RFID-Technologies and Applications (RFID-TA)*, Sitges, Spain, Sep. 2011, pp. 286–291.
- [7] J. Kaitovic, R. Langwieser, and M. Rupp, “A smart collision recovery receiver for RFIDs,” *EURASIP Journal on Embedded Systems*, vol. 2013, no. 7, pp. 1–19, Apr. 2013.
- [8] K. Fyhn, R. M. Jacobsen, P. Popovski, A. Scaglione, and T. Larsen, “Multipacket reception of passive UHF RFID tags: a communication theoretic approach,” *IEEE Trans. Signal Process.*, vol. 59, no. 9, pp. 4225–4237, Sep. 2011.

- 
- [9] J. Wang, H. Hassanieh, D. Katabi, and P. Indyk, “Efficient and reliable low-power backscatter networks,” in *Proc. ACM SIGCOMM*, Helsinki, Finland, Aug. 2012, pp. 61–72.
- [10] G. Vannucci, A. Bletsas, and D. Leigh, “A software-defined radio system for backscatter sensor networks,” *IEEE Trans. Wireless Commun.*, vol. 7, no. 6, pp. 2170–2179, Jun. 2008.
- [11] P. Hu, P. Zhang, and D. Ganesan, “Leveraging interleaved signal edges for concurrent backscatter,” *SIGMOBILE Mob. Comput. Commun. Rev.*, vol. 18, no. 3, pp. 26–31, Jan. 2015.
- [12] —, “Laissez-faire: Fully asymmetric backscatter communication,” *SIGCOMM Comput. Commun. Rev.*, vol. 45, no. 4, pp. 255–267, Aug. 2015.
- [13] J. Ou, M. Li, and Y. Zheng, “Come and be served: Parallel decoding for COTS RFID tags,” *IEEE/ACM Trans. Netw.*, vol. 25, no. 3, pp. 1569–1581, Jun. 2017.
- [14] M. Jin, Y. He, X. Meng, Y. Zheng, D. Fang, and X. Chen, “FlipTracer: Practical parallel decoding for backscatter communication,” *IEEE/ACM Transactions on Networking*, vol. 27, no. 1, pp. 330–343, Feb. 2019.
- [15] M. Jin, Y. He, X. Meng, D. Fang, and X. Chen, “Parallel Backscatter in the wild: When burstiness and randomness play with you,” *IEEE/ACM Transactions on Networking*, vol. 29, no. 1, pp. 65–77, Oct. 2021.
- [16] S. Chen, S. Zhong, S. Yang, and X. Wang, “A multiantenna RFID reader with blind adaptive beamforming,” *IEEE Internet of Things Journal*, vol. 3, no. 6, pp. 986–996, Dec. 2016.
- [17] E. Giannelos, E. Andrianakis, K. Skyvalakis, A. G. Dimitriou, and A. Bletsas, “Robust RFID localization in multipath with phase-based particle filtering and a mobile robot,” *IEEE Journal of Radio Frequency Identification*, 2021, accepted.
- [18] J. F. Ensworth and M. S. Reynolds, “Every smart phone is a backscatter reader: Modulated backscatter compatibility with bluetooth 4.0 low energy (BLE) devices,” in *Proc. IEEE RFID*, San Diego, CA, Apr. 2015, pp. 78–85.
- [19] J. Kimionis, A. Bletsas, and J. N. Sahalos, “Increased range bistatic scatter radio,” *IEEE Trans. Commun.*, vol. 62, no. 3, pp. 1091–1104, Mar. 2014.

- 
- [20] —, “Bistatic backscatter radio for tag read-range extension,” in *Proc. IEEE Int. Conf. on RFID-Technologies and Applications (RFID-TA)*, Nice, France, Nov. 2012.
- [21] —, “Design and implementation of RFID systems with software defined radio,” in *Proc. IEEE European Conf. on Antennas and Propagation (EuCAP)*, Prague, Czech Republic, Mar. 2012, pp. 3464–3468.
- [22] —, “Bistatic backscatter radio for power-limited sensor networks,” in *Proc. IEEE Global Commun. Conf. (Globecom)*, Atlanta, GA, Dec. 2013, pp. 353–358.
- [23] V. Liu, A. Parks, V. Talla, S. Gollakota, D. Wetherall, and J. R. Smith, “Ambient backscatter: Wireless communication out of thin air,” in *Proc. ACM SIGCOMM*, Hong Kong, China, 2013, pp. 39–50.
- [24] P. N. Alevizos, K. Tountas, and A. Bletsas, “Multistatic scatter radio sensor networks for extended coverage,” *IEEE Trans. Wireless Commun.*, vol. 17, no. 7, pp. 4522–4535, Jul. 2018.
- [25] J. D. Griffin and G. D. Durgin, “Gains for RF tags using multiple antennas,” *IEEE Trans. Antennas Propag.*, vol. 56, no. 2, pp. 563–570, Feb. 2008.
- [26] M. Ouroutzoglou, G. Vougioukas, G. N. Karystinos, and A. Bletsas, “Multistatic noncoherent linear complexity Miller sequence detection for Gen2 RFID/IoT,” *IEEE Trans. Wireless Commun.*, 2019, submitted.
- [27] P. V. Nikitin, R. Martinez, S. Ramamurthy, H. Leland, G. Spiess, and K. V. S. Rao, “Phase based spatial identification of UHF RFID tags,” in *Proc. IEEE Int. Conf. on RFID*, Orlando, USA, Apr. 2010, pp. 102–109.
- [28] R. Miesen, F. Kirsch, and M. Vossiek, “Holographic localization of passive UHF RFID transponders,” in *Proc. IEEE Int. Conf. on RFID*, Orlando, USA, Apr. 2011, pp. 32–37.
- [29] E. DiGiampaolo and F. Martinelli, “Mobile robot localization using the phase of passive uhf rfid signals,” *IEEE Trans. Ind. Electron.*, vol. 61, no. 1, pp. 365–376, Jan. 2014.
- [30] T. Liu, L. Yang, Q. Lin, Y. Guo, and Y. Liu, “Anchor-free backscatter positioning for RFID tags with high accuracy,” in *Proc. IEEE Int. Conf. on Computer Communications (Infocom)*, Toronto, Canada, Apr. 2014, pp. 379–387.

- 
- [31] A. Buffi, P. Nepa, and F. Lombardini, “A phase-based technique for localization of UHF-RFID tags moving on a conveyor belt: Performance analysis and test-case measurements,” *IEEE Sensors J.*, vol. 15, no. 1, pp. 387–396, Jan. 2015.
- [32] E. DiGiampaolo and F. Martinelli, “A robotic system for localization of passive UHF-RFID tagged objects on shelves,” *IEEE Sensors J.*, vol. 18, no. 20, pp. 8558–8568, Oct. 2018.
- [33] F. Martinelli, “Simultaneous localization and mapping using the phase of passive UHF-RFID signals,” *Journal of Intelligent & Robotic Systems (JINT)*, vol. 94, no. 3-4, pp. 711–725, Jul. 2019.
- [34] A. Tzitzis, S. Megalou, S. Siachalou, T. Yioultsis, A. Kehagias, E. Tsardoulias, A. Filotheou, A. Symeonidis, L. Petrou, and A. G. Dimitriou, “Phase ReLock - Localization of RFID tags by a moving robot,” in *Proc. IEEE European Conf. on Antennas and Propagation (EuCAP)*, Krakow, Poland, Mar. 2019, pp. 1–5.
- [35] D. Vasicht, S. Kumar, and D. Katabi, “Decimeter-level localization with a single WiFi access point,” in *Proc. USENIX Symposium on Networked Systems Design and Implementation (NSDI)*, Santa Clara, USA, Mar. 2016, pp. 165–178.
- [36] J. Wang and D. Katabi, “Dude, wheres my card? RFID positioning that works with multipath and non-line of sight,” in *Proc. ACM SIGCOMM*, Hong Kong, China, Aug. 2013, pp. 51–62.
- [37] Y. Ma, N. Selby, and F. Adib, “Minding the billions: Ultra-wideband localization for deployed RFID tags,” in *Proc. ACM Int. Conf. on Mobile Computing and Networking (Mobicom)*, Snowbird, USA, Oct. 2017, pp. 248–260.
- [38] M. Kotaru, K. Joshi, D. Bharadia, and S. Katti, “SpotFi: Decimeter level localization using WiFi,” in *Proc. ACM SIGCOMM*, London, United Kingdom, Aug. 2015, pp. 269–282.
- [39] A. Goldsmith, *Wireless Communications*. New York, NY, USA: Cambridge University Press, 2005.
- [40] A. Bletsas, A. G. Dimitriou, and J. N. Sahalos, “Improving backscatter radio tag efficiency,” *IEEE Trans. Microw. Theory Techn.*, vol. 58, no. 6, pp. 1502–1509, Jun. 2010.

- 
- [41] A. Bletsas, J. Kimionis, A. G. Dimitriou, and G. N. Karystinos, “Single-antenna coherent detection of collided FM0 RFID signals,” *IEEE Trans. Commun.*, vol. 60, no. 3, pp. 756–766, Mar. 2012.
- [42] M. Simon and D. Divsalar, “Some interesting observations for certain line codes with application to RFID,” *IEEE Trans. Commun.*, vol. 54, no. 4, pp. 583–586, Apr. 2006.
- [43] D. Koller and N. Friedman, *Probabilistic Graphical Models: Principles and Techniques*. MIT Press, 2009.
- [44] S. Gollakota and D. Katabi, “Zigzag decoding: Combating hidden terminals in wireless networks,” *SIGCOMM Comput. Commun. Rev.*, vol. 38, no. 4, pp. 159–170, Aug. 2008.
- [45] H. Griffiths and C. Baker, *An Introduction to Passive Radar*. Artech, 2017.
- [46] E. Giannelos, “Technical Report, School of ECE, Technical Univ. of Crete,” Jan. 2020.
- [47] K. Skyvalakis, E. Giannelos, E. Andrianakis, and A. Bletsas, “Elliptical DoA estimation and localization,” in *Proc. IEEE Int. Conf. on RFID-Technologies and Applications (RFID-TA)*, 2021, submitted.
- [48] M. Nakagami, “The m-distribution - A general formula of intensity distribution of rapid fading,” in *Statistical Methods in Radio Wave Propagation*. Pergamon, 1960, pp. 3 – 36.
- [49] J. Richter-Gebert, *Perspectives on Projective Geometry: A Guided Tour Through Real and Complex Geometry*, 1st ed. Springer Publishing Company, Incorporated, 2011.